

A thermomechanical cohesive zone model for bridged delamination cracks

Ashwin Hattiangadi, Thomas Siegmund*

School of Mechanical Engineering, 585 Purdue Mall, Purdue University, IN, 47907, USA

Received 2 April 2003; received in revised form 4 August 2003; accepted 5 August 2003

Abstract

The coupled thermomechanical numerical analysis of composite laminates with bridged delamination cracks loaded by a temperature gradient is described. The numerical approach presented is based on the framework of a cohesive zone model. A traction–separation law is presented which accounts for breakdown of the micromechanisms responsible for load transfer across bridged delamination cracks. The load transfer behavior is coupled to heat conduction across the bridged delamination crack. The coupled crack–bridging model is implemented into a finite element framework as a thermomechanical cohesive zone model (CZM). The fundamental response of the thermomechanical CZM is described. Subsequently, bridged delamination cracks of fixed lengths are studied. Values of the crack tip energy release rate and of the crack heat flux are computed to characterize the loading of the structure. Specimen geometries are considered that lead to crack opening through bending deformation and buckling delamination. The influence of critical mechanical and thermal parameters of the bridging zone on the thermomechanical delamination behavior is discussed. Bridging fibers not only contribute to crack conductance, but by keeping the crack opening small they allow heat flux across the delamination crack to be sustained longer, and thereby contribute to reduced levels of thermal stresses. The micro-mechanism based cohesive zone model allows the assessment of the effectiveness of the individual mechanisms contributing to the thermomechanical crack bridging embedded into the structural analysis. © 2003 Elsevier Ltd. All rights reserved.

Keywords: Crack bridging; Crack conductance; Thermomechanical loading; Cohesive zone model; Buckling delamination

* Corresponding author. Tel.: 765-494-9766; fax: 765-496-7536.
E-mail address: siegmund@ecn.purdue.edu (T. Siegmund).

1. Introduction

Fiber reinforced ceramic matrix composites (CMC) are used in a variety of applications where both mechanical as well as thermal material properties are of concern. In many cases structures of interest are subjected to conditions of high heat flux. Examples of engineering components using CMC parts are thermal protection systems for space vehicles (Dimitrienko, 1999), actively cooled first wall fusion reactor liners (Tivey et al., 1999), as well as shell structures in propulsion systems (Brockmeyer, 1993; John et al., 1999), and high performance brakes (Krenkel and Henke, 1999). Heat fluxes with up to 150 MW/m^2 are expected to occur in certain applications (Tivey et al., 1999). CMCs are attractive for these applications since they offer thermal stability and flexibility in microstructural design by adapting fiber volume fractions and fiber orientations distributions to best fit a specific component. Crack bridging due to fibers extending across a delamination crack plays an important role in the behavior of CMCs. This mechanism provides an efficient way to increase toughness for most fiber architectures and modes of loading (Thouless and Evans, 1988; Sbaizero et al., 1990; Spearing and Evans, 1992; Dransfield et al., 1994; Cox, 1994; Mouritz and Cox, 2000).

Under thermal loads, delamination cracks are discontinuities in the temperature field and impede heat flow. The redistribution of temperature leads to local thermal stresses at the crack tip in addition to the thermal stress due to the constraints imposed on the external surface. The presence of fiber bridging is also beneficial as heat flux is considered (Donaldson et al., 1998), leading to increased heat flux and thus reduces the thermal stresses at the crack tip. Early investigations on the influence of the heat flux conditions on the behavior of cracked structures were conducted by Florence and Goodier (1959, 1963) and Sih (1962). These studies were concerned with conditions of steady state and remote uniform heat flux, and assumed fully isolated cracks in infinite homogeneous isotropic bodies. The results of these studies, and of subsequent others by Barber (1979) and Chen and Huang (1992), demonstrated that the energy release rate associated with thermal effects could indeed be substantial. Later, Hasebe et al. (1986), Lee and Shul (1991), Itou (1993), Yan and Ting (1993), Chao and Chang (1994) and Lee and Park (1995), extended the linear-elastic fracture mechanics analyses to cracks at bi-material interfaces as well as to arbitrary cracks geometries. Crack heat flux was included into the analyses by Barber and Comninou (1983), Martin-Moran et al. (1983), Kuo (1990) and Hutchinson and Lu (1995). Applications were also undertaken to study interface cracks in high-temperature coatings under steady state temperature conditions (Lee and Erdogan, 1998; Qian et al., 1998; Miller and Chona, 1998; Hutchinson and Evans, 2002). Results showed a significant dependence of the energy release rate on the assumed crack conductance. However, the crack conductance was commonly assumed as constant, not only along the entire crack but also independent of crack opening, and rarely based on physically motivated input. Such simplifying assumptions become even less valid for the CMC system of interest here, where bridging fibers contribute both to the load and the heat transfer across the delamination crack over an extended fracture process zone. Recently, an investigation of crack heat flux in composites was conducted in McDonald et al. (2000). This study laid special emphasis on the effects of crack opening on the thermal conductance of delamination cracks in composites.

Experiments to measure crack conductance were performed by use of a phase-sensitive photo-thermal technique, and a crack conductance model was developed. The outcome of the study clearly points to the necessity to incorporate a correct description of the crack conductance into failure predictions. Nevertheless, no studies have yet been presented that combine the stress analysis of cracked laminates including the computation of energy release rates with detailed description of the crack conductance.

In the present study mechanical crack bridging and crack heat transfer is accounted for in a coupled thermomechanical analysis by use of a thermomechanical cohesive zone model (CZM) approach (Hattiangadi and Siegmund, 2002). The cohesive zone model incorporates a detailed description of the processes occurring during crack bridging (Cox, 1999), i.e. fiber pull-out, matrix spalling and fiber breakage. Thereby, the cohesive constitutive relations derived here extend earlier work by Llorca and Elices (1992) and Kaute et al. (1993) to mixed-mode loading condition. In the thermal part, the cohesive zone model incorporates a description of crack conductance in dependence of the current local condition within the bridged crack. The current state of fiber bridging, the presence of gas entrapped in the delamination crack as well as radiative heat transfer determine the cohesive zone conductance. The thermomechanical cohesive zone model provides additional coupling between thermal and stress analysis beyond thermal stresses as material deterioration taking place in the bridging zone leads to changes both in load and heat transfer across the delamination crack. The thermomechanical cohesive zone model is implemented within the finite element method. This approach provides a convenient framework for the analysis of material separation processes (Barenblatt, 1962; Needleman, 1987). The finite element implementation bears some resemblance to the thermomechanical contact formulations of Zavarise et al. (1992) and Pantusa et al. (2000).

Within the micromechanics approach adopted for the description of the crack bridging process no traction–separation law needs to be specified. A cohesive strength, a cohesive zone heat flux, and corresponding cohesive length parameters characteristic of the bridging process are directly obtained from simulation. Commonly, studies of crack bridging generally are performed in two separate stages. First, the determination of the crack bridging law is undertaken, and subsequently a structural analysis with a simplified traction–separation law is performed. With the present thermomechanical cohesive zone model such a separation into two steps of analysis with different levels of refinement is no longer needed. The thermomechanical cohesive zone model is applied in a numerical study of the mechanics of bridged delamination cracks in a unidirectional reinforced CMC laminate subjected to thermal gradient loading. Effects of specimen geometry, crack environments and the micromechanics of load transfer across the crack are investigated.

2. Formulation

2.1. Thermomechanical cohesive zone model formulation

For a solution of the coupled thermomechanical problem of a solid containing bridged delamination cracks, both mechanical equilibrium and energy balance must be fulfilled.

In the present approach, cracks are considered as internal cohesive surfaces with partial load and heat transfer capabilities. In view of the finite element approximation, the mechanical equilibrium equation includes the contribution of the cohesive zone through integrals over the internal surfaces, S_{int} . The principle of virtual work is written as

$$\int_V \mathbf{s} : \delta \mathbf{F} dV - \int_{S_{\text{int}}} \mathbf{T}_{\text{CZ}} \cdot \delta \Delta dS = \int_{S_{\text{ext}}} \mathbf{T}_e \cdot \delta \mathbf{u} dS \quad (1)$$

with the nominal stress tensor, $\mathbf{s} = \mathbf{F}^{-1} \det(\mathbf{F}) \boldsymbol{\sigma}$, the Cauchy stress, $\boldsymbol{\sigma}$, the deformation gradient, \mathbf{F} , and the displacement vector, \mathbf{u} . Traction vectors are related to $\boldsymbol{\sigma}$ by $\mathbf{T} = \mathbf{n} \boldsymbol{\sigma}$, with \mathbf{n} being the surface normal. \mathbf{T}_e is the traction vector on the external surface of the body. The cohesive zone contribution on the internal surface, S_{int} , are given by the cohesive surface traction, \mathbf{T}_{CZ} , and the displacement jump across the cohesive surface, $\Delta = (\Delta_n \mathbf{n} + \Delta_t \mathbf{t}) = \mathbf{u}_+ - \mathbf{u}_-$, where $i = +, -$ represent top and lower surfaces, with \mathbf{u}_+ and \mathbf{u}_- the displacements of two initially bonded points on opposite crack surfaces.

The energy balance including the contribution of the cohesive zone on the internal surfaces, written in variational form for steady state and using Fourier's law, is expressed by

$$\int_V \frac{\partial \delta \theta}{\partial x} \mathbf{k} \frac{\partial \delta \theta}{\partial x} dV - \int_{S_{\text{int}}} q_{\text{CZ}} \delta(\Delta \theta) dS = \int_{S_{\text{ext}}} \delta \theta q_e dS \quad (2)$$

with the temperature, θ , the conductivity matrix, \mathbf{k} , and the heat flux per external unit area into the body, q_e . The cohesive zone contributions are described by the integral over the internal surface, S_{int} , as the product of the cohesive zone heat flux, q_{CZ} , and the temperature jump across the cohesive surface, $\Delta \theta = \theta_+ - \theta_-$.

The implementation of the mechanical part of the cohesive elements requires the evaluation of the derivative of the second term of Eq. (1). The virtual work of the cohesive forces, δU_m , can be expressed in terms of the normal and tangential components of tractions and displacement jumps as

$$\delta U_m = \int_{S_{\text{int}}} [T_n \ T_t] [\delta \Delta_n \ \delta \Delta_t]^T dS. \quad (3)$$

Substituting the virtual displacement jumps in terms of the cohesive element nodal shape functions, the first variation of δU_m is

$$d\delta U_m = \int_{S_{\text{int}}} [dT_n \ dT_t] \cdot \delta \mathbf{A}_m dS, \quad (4)$$

where $\delta \mathbf{A}_m = \mathbf{N}_m \cdot \delta \Delta$ and \mathbf{N}_m are cohesive element nodal shape function for mechanical terms. The incremental normal and tangential tractions, dT_n and dT_t , are related to incremental displacement jumps by the cohesive zone Jacobian, \mathbf{J}_m ,

$$\begin{Bmatrix} dT_n \\ dT_t \end{Bmatrix} = \mathbf{J}_m : \begin{Bmatrix} d\Delta_n \\ d\Delta_t \end{Bmatrix}, \quad (5a)$$

$$\mathbf{J}_m = \begin{bmatrix} \frac{\partial T_n}{\partial \Delta_n} & \frac{\partial T_n}{\partial \Delta_t} \\ \frac{\partial T_t}{\partial \Delta_n} & \frac{\partial T_t}{\partial \Delta_t} \end{bmatrix}, \quad (5b)$$

Expressing the incremental tractions in Eq. (4) by use of \mathbf{J}_m , and writing the incremental displacement jump by use of the incremental cohesive element nodal displacement jump leads to the mechanical part of the tangent stiffness matrix, \mathbf{K}_m :

$$\mathbf{K}_m = \int_{S_{int}} \mathbf{N}_m^T : \mathbf{J}_m : \mathbf{N}_m dS. \quad (6)$$

In addition to the mechanical terms, the implementation of the thermomechanical cohesive element requires the evaluation of the first variation of the second term in the internal energy expressed in Eq. (2). The term, δU_{th} , is expressed via the virtual temperature jump as

$$\delta U_{th} = \int_{S_{int}} q_{CZ} \delta(\Delta\theta) dS. \quad (7)$$

The first variation of δU_{th} has the form

$$d\delta U_{th} = \int_{S_{int}} dq_{CZ} \delta(\Delta\theta) dS, \quad (8)$$

where dq_{CZ} is the incremental cohesive zone heat flux related to the increments in the jump in temperature and displacement across the cohesive zone:

$$\{dq_{CZ}\} = \begin{bmatrix} \frac{\partial q_{CZ}}{\partial \Delta_n} & \frac{\partial q_{CZ}}{\partial \Delta_t} & \frac{\partial q_{CZ}}{\partial \theta_i} \end{bmatrix} \begin{Bmatrix} d\Delta_n \\ d\Delta_t \\ d\theta_i \end{Bmatrix}, \quad i = +, -. \quad (9)$$

The cohesive zone flux, q_{CZ} , is the product of cohesive zone conductance, h_{CZ} , and the temperature jump,

$$q_{CZ} = h_{CZ} \Delta\theta. \quad (10)$$

Then, the right hand side of Eq. (9) can be further expressed as

$$\{dq_{CZ}\} = \begin{bmatrix} \frac{\partial h_{CZ}}{\partial \Delta_n} \Delta\theta & \frac{\partial h_{CZ}}{\partial \Delta_t} \Delta\theta & h_{CZ} + \frac{\partial h_{CZ}}{\partial \theta_i} \end{bmatrix} \begin{Bmatrix} d\Delta_n \\ d\Delta_t \\ d\theta_i \end{Bmatrix}. \quad (11)$$

Hence, the first variation of the virtual internal energy in terms of virtual temperature difference takes the form

$$\begin{aligned} d\delta U_{th} = & \int_{S_{int}} \begin{bmatrix} \frac{\partial h_{CZ}}{\partial \Delta_n} & \frac{\partial h_{CZ}}{\partial \Delta_t} \end{bmatrix} [d\Delta_n \ d\Delta_t]^T \delta(\Delta\theta) dS \\ & + \int_{S_{int}} \left(h_{CZ} + \frac{\partial h_{CZ}}{\partial \theta_i} \right) d\theta_i \delta(\Delta\theta) dS. \end{aligned} \quad (12)$$

The first variation of U_{th} can be further expressed in terms of the nodal shape functions as

$$\begin{aligned} d\delta U_{th} = & \int_{S_{int}} \left[\frac{\partial h_{CZ}}{\partial \Delta_n} \frac{\partial h_{CZ}}{\partial \Delta_t} \right] [d\Delta_n \ d\Delta_t]^T \cdot \delta \mathbf{A}_{tm} dS \\ & + \int_{S_{int}} \left(h_{CZ} + \frac{\partial h_{CZ}}{\partial \theta_i} \right) d\theta_i \delta A_{th} dS, \end{aligned} \quad (13)$$

where $\delta \mathbf{A}_{tm} = \mathbf{N}_{tm} \cdot \delta \Delta \theta$, $\delta A_{th} = N_{th} \delta \Delta \theta$ and \mathbf{N}_{tm} and N_{th} are cohesive element nodal shape functions for the coupling terms and the thermal part, respectively. The first term on the right hand side denotes the coupling between cohesive zone conductance and displacement jump, and the second term is due to the temperature dependence of the cohesive zone conductance. The coupling between thermal and mechanical equations is expressed in terms of the Jacobian, \mathbf{J}_{tm} , and the thermal part is expressed in terms of J_{th} ,

$$\{dq\}_{tm} = \mathbf{J}_{tm} \cdot \begin{Bmatrix} d\Delta_n \\ d\Delta_t \end{Bmatrix}, \quad (14a)$$

$$\mathbf{J}_{tm} = \begin{bmatrix} \frac{\partial h_{CZ}}{\partial \Delta_n} & \frac{\partial h_{CZ}}{\partial \Delta_t} \end{bmatrix}, \quad (14b)$$

$$\{dq\}_{th} = J_{th} \{d\theta_i\}, \quad (15a)$$

$$J_{th} = \left[h_{CZ} + \frac{\partial h_{CZ}}{\partial \theta_i} \right]. \quad (15b)$$

Writing the incremental heat flux in Eqs. (14) and (15) in terms of the Jacobians, \mathbf{J}_{tm} , J_{th} , and the incremental temperature jumps, leads to the thermomechanical, \mathbf{K}_{tm} , and thermal, K_{th} , contribution of the tangent stiffness matrix of the cohesive zone element in the form

$$\mathbf{K}_{tm} = \int_{S_{int}} \mathbf{J}_{tm} : \mathbf{N}_m^T : \mathbf{N}_{tm} dS, \quad (16a)$$

$$K_{th} = \int_{S_{int}} J_{th} N_{th}^T N_{th} dS. \quad (16b)$$

Combining the mechanical, coupling and thermal parts from Eqs. (6) and (16), the tangent stiffness matrix, \mathbf{K}_{CZ} , for a single node neglecting the temperature dependence of the mechanical properties of the cohesive zone, can be expressed as

$$\mathbf{K}_{CZ} = \begin{bmatrix} \mathbf{K}_{m\{2 \times 2\}} & 0 \\ \mathbf{K}_{tm\{1 \times 2\}} & K_{th\{1 \times 1\}} \end{bmatrix}_{\{3 \times 3\}}. \quad (17)$$

The numerical implementation of the cohesive zone model uses four node elements with linear interpolation functions for the displacement jumps, and nodal values for temperature jumps across the crack, see Appendix A for the nodal shape functions. The thermomechanical cohesive zone element has been implemented into the finite element program **ABAQUS v6.3.1** through the UEL capability.

2.2. Load transfer

In unidirectional reinforced laminates delamination cracks parallel to the reinforcement axis are commonly bridged by fibers, see Fig. 1(a). Three mechanisms are responsible for load transfer characteristics across bridged delamination cracks, i.e.:

- (i) fiber pull-out,
- (ii) matrix spalling—the growth of cracks in the matrix due to stress concentrations caused by the presence of the bridging fibers,
- (iii) fiber fracture due to combined bending and axial loading, with a Weibull distribution describing the fiber failure statistics.

The model describing the load transfer across the fiber bridging zone is an extension of the mode I crack bridging model of Kaute et al. (1993). The present work generalizes this model to deal with arbitrary values of mode mixity.

Fig. 1(a) depicts the geometry and the main parameters used in the development of the cohesive zone model. The normal and tangential cohesive zone tractions, $T_n(\Delta)$ and $T_t(\Delta)$, can be related to the force per fiber in the normal and tangential direction, $f_n(\Delta)$ and $f_t(\Delta)$, and the number of fibers per unit area of the crack, $n(\Delta)$:

$$T_n(\Delta) = n(\Delta)f_n(\Delta) \quad \text{and} \quad T_t(\Delta) = \frac{n(\Delta)}{2} f_t(\Delta). \quad (18)$$

The factor 1/2 in the equation for T_t takes into account that during crack opening the bridging fibers appear in criss-cross geometry with only half the number of fibers contributing to the tangential load transfer in either direction.

Under application of load, fibers debond from the matrix over a length x_d and subsequently are pulled out. The present model assumes a negligible debonding energy at the fiber–matrix interface, a constant interface sliding stress, and average interface shear stresses. The resulting pull-out stress, $\sigma_p(\Delta)$, acting at the location where the fiber enters the matrix can then be determined from equilibrium to be

$$\sigma_p(\Delta) = \frac{4\tau x_d}{d}, \quad (19)$$

where d is the fiber diameter, and τ is the interface sliding stress. The fiber slippage length, $x_s(\Delta)$, is calculated from the average stress, $\sigma_p(\Delta)/2$, acting over the debonding zone and the debonding length, x_d , as

$$x_s(\Delta) = \frac{\sigma_p(\Delta)}{2E_f} x_d, \quad (20)$$

where E_f is the fiber modulus. As the crack opening increases, the strain $\varepsilon_f(\Delta)$ in the fiber is reduced due to the fiber slippage. The stress in the fiber due to pull-out can then be expressed by

$$\sigma_f(\Delta) = E_f \left(\frac{l(\Delta) - l_0}{l_0} - \frac{2x_s}{l_0} \right), \quad (21)$$

where $l(\Delta)$ is the current and l_0 the initial bridging length. If fiber slippage is extensive, the right hand side of Eq. (21) will dominate. The left hand side—corresponding to the

stress expected if the fiber is tightly gripped (i.e. no debonding)—can be neglected in this case, $\sigma_f(\Delta)=0$. Expressing the current bridging length as $l(\Delta)=\sqrt{(l_0 + \Delta_t)^2 + \Delta_n^2}$, and substituting Eq. (20) into (21), $\sigma_p(\Delta)$ can be obtained as a function of material properties, E_f, d, τ, l_0 and the values of the normal and tangential displacement jump:

$$\sigma_p(\Delta) = \sqrt{\frac{4\tau E_f}{d}} \left[\sqrt{(l_0 + \Delta_t)^2 + \Delta_n^2} - l_0 \right]. \quad (22)$$

From the stress, $\sigma_p(\Delta)$, given by the fiber pull-out model, the components of the force carried per bridging fiber in normal and tangential direction, f_n and f_t , are calculated as

$$f_n(\Delta) = \sigma_p(\Delta) \frac{\pi d^2}{4} \tan \varphi \quad \text{and} \quad f_t(\Delta) = \sigma_p(\Delta) \frac{\pi d^2}{4}, \quad (23)$$

where φ is angle between the bridging fibers and the crack surface.

As the displacement jump across the crack increases, the forces carried by the bridging fibers increase until spalling of the matrix initiates and imposes an upper limit on the forces that can be carried by the fibers. An approximate expression linking the maximum value of the normal component of the fiber force, $\max(f_n)$, to the fracture toughness of the matrix, K_{IC}^m (Kaute et al., 1993), can be obtained based on results of Tada et al. (1973) as

$$\frac{\max(f_n)}{\beta \hat{a}} = K_{IC}^m \sqrt{\pi \hat{a}}, \quad (24)$$

where $2\hat{a}$ is the length of cracks extending to either side of a fiber and $\beta \hat{a}$ is the mean crack length parallel to the fiber over which the forces f_n acts. Fig. 1(b) depicts the details of the geometric quantities used in the description of the spalling process.

During matrix spalling a crack can propagate catastrophically from the weak fiber matrix interface. Therefore, it may seem reasonable to link the critical crack-length, \hat{a}_c , beyond which matrix spalling occurs to the mean distance, L , between two neighboring fibers as $\hat{a}_c=L-d/2$. In the case of parallel fibers, the distance L and the fiber diameter d are related through the fiber volume fraction V_f :

$$\hat{a}_c = d \left[\sqrt{\frac{\pi}{2\sqrt{3}}} \frac{1}{\sqrt{V_f}} - \frac{1}{2} \right]. \quad (25)$$

Combining Eqs. (23)–(25) leads to a prediction of $\max(f_n)$. Further crack opening occurs under constant values of f_n and f_t as well as of φ . The maximum value of φ is obtained at the onset of spalling by inverting (22) and substituting $\max(f_n)$ for f_n .

$$\varphi_{sp} = \max(\varphi) = \tan^{-1} \left[\frac{4 \max(f_n)}{\sigma_p(\Delta) \pi d^2} \right]. \quad (26)$$

The number of bridging fibers per unit area initially bridging the crack is n_0 . As loading progresses this number subsequently diminishes due to the occurrence of fiber fracture. A Weibull statistics approach is used to predict the number of surviving fibers in the bridging zone. Fiber fracture is due to combined bending-axial loading. Using the result of Kaute et al. (1993) the bending stress can be expressed in terms of the

angle, φ , and fiber modulus, E_f :

$$\sigma_b = \frac{E_f \tan^2 \varphi}{2\delta/d} \quad (27)$$

where δ is the asymptotic distance of the fiber with reference to its axial direction, see Fig. 1(a). For the calculation of the bending stress, the ratio δ/d is assumed to be close to unity ($\delta/d = 0.9$).

The combined stress due to tension in fibers during pull-out and bending at the root of the bridged fiber is $\bar{\sigma}(\Delta) = \sigma_p(\Delta) + \sigma_b$. Prior to matrix spalling the survival probability is given as

$$p_s = \exp \left[-C_b \frac{l(\Delta)}{l_{\text{ref}}} \left(\frac{\bar{\sigma}(\Delta)}{\sigma_{\text{ref}}} \right)^m \right] \quad (28)$$

where l_{ref} and σ_{ref} are Weibull reference length and strength, respectively and m is the Weibull modulus. C_b is a dimensionless correction factor, ($C_b < 1$), to allow for the comparison between bending and tensile stresses. As matrix spalling occurs, the survival probability defined in Eq. (28) is modified. As the bridging angle, $\varphi = \varphi_{\text{sp}}$, the spanning length $l(\Delta)$ in Eq. (28) is expressed in terms of the normal displacement jump, Δ_n , as $l = \Delta_n \sin \varphi_{\text{sp}}$. Also, the bending stress, σ_b , reaches a maximum value when matrix spalling occurs. The number of bridging fibers per unit area is given as,

$$n(\Delta) = n_0 p_s(\Delta). \quad (29)$$

Finally, the traction–separation behavior in Eq. (18) is the outcome of combining Eqs. (23), (24) and (29) which contain the material property information. The derivatives of tractions with respect to displacement jumps as needed in the Jacobian, Eq. (5), are presented in Appendix B.

2.3. Heat transfer

Heat flux across the cohesive zone, q_{CZ} , is described as a product of the temperature jump across the crack, $\Delta\theta$, and the cohesive zone conductance, h_{CZ} . In developing the thermal part of the thermomechanical cohesive zone law the following simplifying assumptions are made:

- (i) One-dimensional heat transfer across the crack is considered and described by a thermal resistor model,
- (ii) Thermal resistance in the fiber debonding zone and constriction effects at locations where the fiber emerges from the matrix are neglected,

The heat flux across the cohesive zone is the sum of the heat fluxes due to conduction through the bridging fibers, q_f , the gas trapped in the crack, q_g , and the radiation between the crack surfaces, q_r ; Fig. 1(c). The cohesive zone conductance model combines the conductance of gas, fiber and radiation by a parallel arrangement of resistors, as shown in Fig. 1(d), Donaldson et al. (1998), McDonald et al. (2000):

$$h_{\text{CZ}} = h_f + h_g + h_r. \quad (30)$$

The conductance through fiber, h_f , depends on the current bridging length, l , which can be expressed in terms of the displacement jump, Δ , the bridging angle, φ , and the volume fraction of bridging fibers in the crack, V_f^C . The model assumes a linear temperature dependence of the thermal conductivity of the fibers, $k_f + C_f(\theta)$, in dependence of the average temperature of the upper and lower crack surface. The contribution of the fibers to the cohesive zone conductance, h_f , is expressed as

$$h_f(\Delta, \theta_+, \theta_-) = V_f^C \left[k_f + C_f \left(\frac{\theta_+ + \theta_-}{2} \right) \right] \frac{\sin \varphi}{\Delta_n}. \quad (31)$$

The conductivity of the gas trapped in the crack, h_g , depends on the temperature dependent thermal conductivity of the gas, $k_g + C_g(\theta)$, the displacement jump across the crack and the volume fraction of gas in the crack, $(1 - V_f^C)$:

$$h_g(\Delta, \theta_+, \theta_-) = (1 - V_f^C) \left[k_g + C_g \left(\frac{\theta_+ + \theta_-}{2} \right) \right] \frac{1}{\Delta_n}. \quad (32)$$

The contribution to the cohesive zone conductance due to radiation, h_r , is dependent on the crack surface temperatures

$$h_r(\theta_+, \theta_-) = \frac{S_b}{2/e_m - 1} [(\theta_+ - \theta_0) + (\theta_- - \theta_0)][(\theta_+ - \theta_0)^2 + (\theta_- - \theta_0)^2] \quad (33)$$

with the Stephan Boltzman constant, $S_b = 5.67 \times 10^{-8} \text{ W/m}^2\text{K}^4$, an assumed emissivity of the crack surfaces of, $e_m = 1.0$, and the reference temperature, θ_0 .

In describing the cohesive zone conductance, the current volume fraction of fibers in the cohesive zone, V_f^C , is to be defined. This quantity depends on the fiber diameter, the displacement jump across the cohesive zone, the bridging length, and the number of fibers in the cohesive zone. Combining these quantities, the volume fraction of fibers in the cohesive zone is expressed as

$$V_f^C = n_0 p_s \frac{d^2 \pi l_0}{4 \Delta_n}. \quad (34)$$

In deriving Eq. (34) the change of the bridging length during spalling was neglected. An upper limit for the value of V_f^C is assumed as $\max(V_f^C) = \pi/4$. The thermal resistor model is irreversible by being coupled to the mechanical part of the cohesive zone model. The relative contributions of fibers and gas to h_{CZ} change as material deterioration progresses.

The derivatives of the cohesive zone conductance with respect to the temperature jump as well as the derivatives of the cohesive zone conductance with respect to the displacement jump as needed in the Jacobian, Eqs. (14) and (15) are presented in Appendix C.

3. Basic cohesive zone response

3.1. Material properties

In this investigation the thermomechanical cohesive zone model is applied to a study of a CMC consisting of unidirectional aligned SiC fibers in an Al_2O_3 matrix. Two sets

Table 1
Material properties of Al_2O_3 (matrix) and SiC (fiber)

θ [K]	E_m [GPa]	E_f [GPa]	ν_m	ν_f	k_m [W/mK]	k_f [W/mK]	α_m [10^{-6} K^{-1}]	α_f [10^{-6} K^{-1}]
300	420	180	0.23	0.2	33	1.25	6.7	3.2
573	405	170	0.233	0.2	18	1.7	7.5	4.1
873	390	157	0.237	0.2	12	2.25	8.0	4.8
1500	355	140	0.247	0.2	7	3.4	8.3	5.2

Table 2
Effective properties of the Al_2O_3 –SiC composite

θ [K]	E_T [GPa]	E_L [GPa]	G_T [GPa]	G_L [GPa]	ν_T	ν_L	k_T [W/mK]	k_L [W/mK]	α_T [10^{-6} K^{-1}]	α_L [10^{-6} K^{-1}]
300	392.7	346.7	121.5	137.4	0.43	0.17	18.64	23.47	7.56	5.62
573	376.5	333.2	116.2	131.7	0.43	0.17	10.84	13.11	8.29	6.49
873	358.9	318.8	110	125.4	0.43	0.17	7.91	9.07	8.67	7.1
1500	324.3	289.1	98.8	112.9	0.43	0.18	5.68	5.92	8.89	7.48

of material parameters are required for the description of the material within the current approach.

The continuum properties of the composite are calculated from fiber and matrix properties. The temperature dependent thermomechanical material properties for typical SiC fibers and an Al_2O_3 matrix of 96% density are given in Table 1(a) based on published data in Touloukian (1967), Brennan et al. (1982), Simon and Bunsell (1984), Li and Bradt (1987), Heredia et al. (1995), Lu and Hutchinson (1995) and Munro (1997). Based on these properties, the effective properties of a composite with a volume fraction of $V_f = 0.3$ were calculated by use of the Mori-Tanaka and Hatta-Taya theories, see (Nemat-Nasser and Hori, 1999; Nadeau and Ferrari, 1999; Hatta and Taya, 1985). The temperature dependent effective properties obtained by these procedures are summarized in Table 1(b).

The thermomechanical CZM requires information on the fiber, the matrix, the fiber-matrix interface properties, statistical information on fiber failure, and the thermal conductivity of the gas considered. The default parameters used in the present study are given in Table 2, compiled from data given in Kaute et al. (1993, 1995), Lu and Hutchinson (1995), Heredia et al. (1995) and Munro (1997).

3.2. Mechanical response of the cohesive zone model

The basic response behavior of the thermomechanical cohesive zone model is documented for loading under the conditions of uniform displacement and temperature jumps across the cohesive zone. Such simulations were accomplished by combining

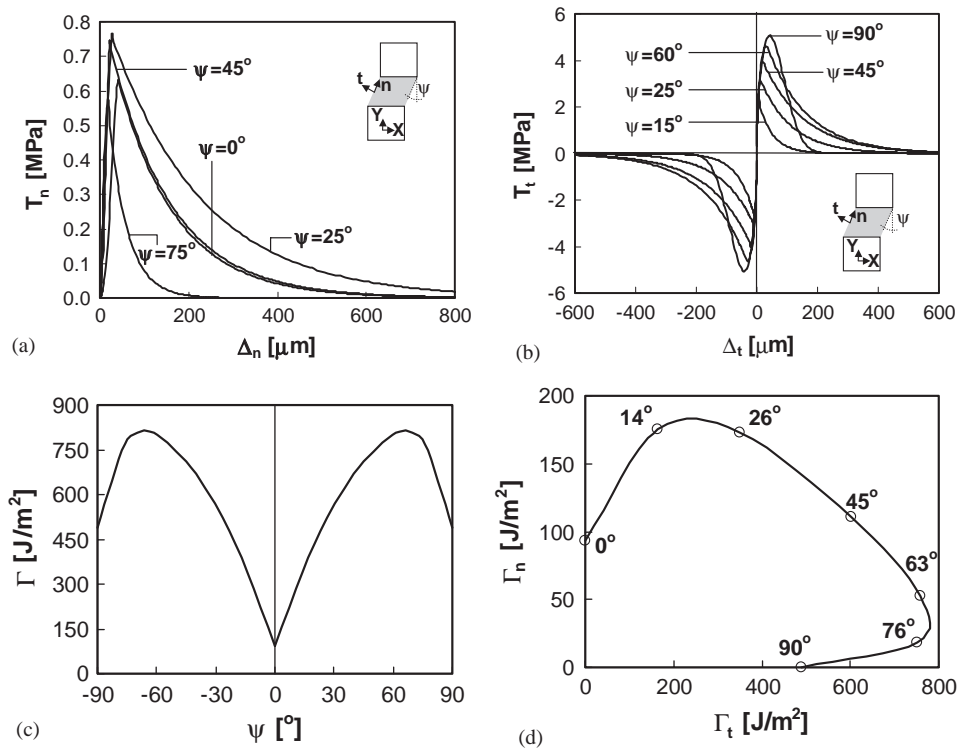


Fig. 2. Predicted traction–separation response: (a) normal and (b) shear components; (c) cohesive energy vs. mode mixity; (d) envelope of Γ_n and Γ_t .

a single cohesive zone element with two plain strain temperature–displacement solid elements.

The predicted normal and tangential tractions as a function of the displacement jumps for a range of mode mixities are shown in Fig. 2(a) and (b). The basic outcome of the cohesive zone model is a traction–separation curve that initially requires increasing load for material separation, then reaches a maximum traction value, and subsequently leads to a gradual loss in load carrying capacity. Positive and negative tangential tractions are possible since the bridging fibers are assumed to be present in a criss-cross arrangement within the cohesive zone. The maximum traction values reached can be interpreted as a cohesive strength. The displacement jump at the point where traction drops to near zero due to the survival probability of fibers approaching zero can be identified as mechanical cohesive length. Then, the present model shows the same characteristics as commonly used prescribed traction–separation laws.

For the material parameters used in the analysis, the predicted normal cohesive strengths are in the range of 0.5 to 0.75 MPa for low values of the mode mixity, $\psi = \tan^{-1}(\Delta_t/\Delta_n)$. As ψ approaches 90° the normal cohesive strength decreases and becomes negligible. The predicted normal mechanical cohesive lengths range between

600 to 900 μm for low values of mode mixity, but drop to small values as the mode mixity approaches 90° .

The predicted traction–separation response in tangential direction, $T_t - \Delta_t$, shows the same basic characteristics as the $T_n - \Delta_n$ response. While the range of predicted tangential mechanical cohesive length values is smaller to those for the normal cohesive zone response, the predicted tangential cohesive strengths are considerably larger than the normal cohesive strengths. As the mode-mixity ratio increases, the predicted maximum value of the tangential cohesive strength increases monotonically from 2.0 MPa for $\psi = 15^\circ$ to around 5 MPa obtained for $\psi = 90^\circ$. The predicted tangential mechanical cohesive length values change non-monotonically with mode mixity. They increase from 200 μm at low values of mode mixity, reach a maximum 600 μm of at $\psi = 60^\circ$, and subsequently reduce to 200 μm for $\psi = 90^\circ$.

The change in the traction–separation behavior with increasing mode mixity can be contributed to the competition between failure due to matrix–fiber interface debonding and spalling. For low values of mode mixity, matrix spalling limits the tractions in the cohesive zone. Bending deformation of the fibers is significant, leading to a relative compliant cohesive zone response with a slow breakdown of the survival probability of the fibers. For increasing values of ψ load transfer is dominated by axial loading of the fibers. Fiber–matrix debonding instead of matrix spalling limits the cohesive zone tractions. For the present set of parameter values, the fiber strength is high thus leading to the observed larger cohesive strength values as ψ increases. As the axial load component is significant the compliance of the cohesive zone is reduced, a rapid drop in survival probability of the fibers occurs once fiber fracture sets in. Thus, a fast decay in tractions is present resulting in small values of the tangential mechanical cohesive lengths in case of high mode mixities.

The non-monotonic change in the traction–separation behavior predicted here is in agreement with the results of several experimental investigations of material systems with similar microstructure. The cohesive energy, $\Gamma(\psi)$, characterizing the toughness of the bridging zone is calculated as

$$\Gamma = \Gamma_n + \Gamma_t = \int T_n d\Delta_n + \int T_t d\Delta_t. \quad (34)$$

Cohesive energies in dependence of the mode mixity are given in Fig. 2(c). Data in this plot represent the energy per crack area to advance the bridged crack considered in the subsequent sections. The cohesive energy exhibits similar response to mode mixity behavior used in composite damage models, e.g. by Jansson and Larsson (2001). The cohesive zone energy data are again plotted in Fig. 2(d), in terms of the envelope of $\Gamma_t - \Gamma_n$. The predicted $\Gamma_t - \Gamma_n$ envelope matches well with experimental failure data, as e.g. determined for laminated composites by Partridge and Singh (1995), Benzeggagh and Kenane (1996), Ducept et al. (1997) and Rikards et al. (1998).

3.3. Thermal response of the cohesive zone model

The basic response of the cohesive zone model to thermomechanical loading is demonstrated for cases in which a constant prescribed temperature jump ($\Delta\theta = 1200\text{ K}$)

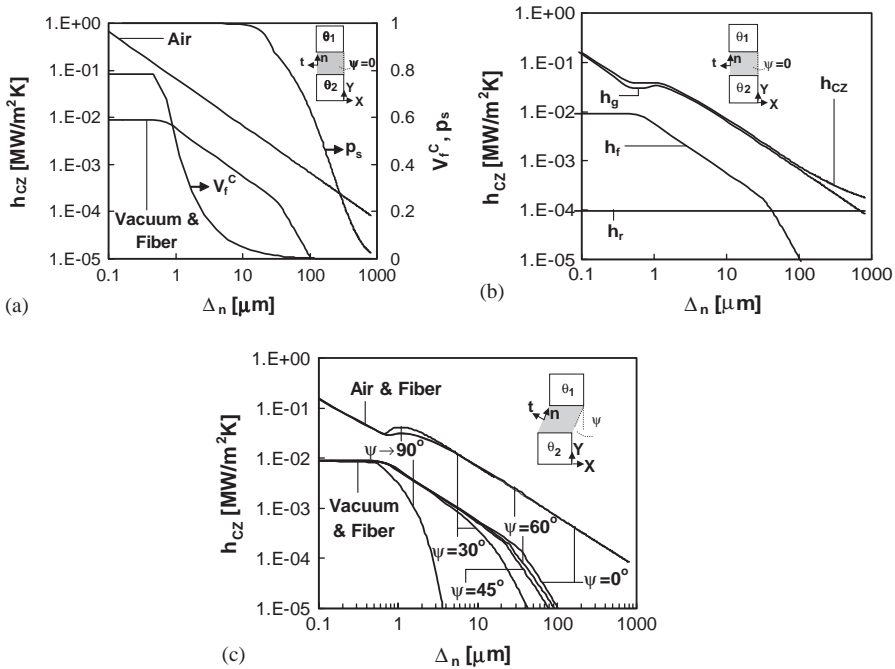


Fig. 3. Predicted cohesive zone conductance: (a) dependence on normal separation for different crack environment, corresponding survival probability and volume fraction of fibers in crack; (b) contribution the cohesive zone conductance by fibers, h_f , gas, h_g , and radiation, h_r ; (c) influence of mode mixity.

across the cohesive zone, and increasing displacement jumps are prescribed. The reference temperature is $\theta_0 = 300$ K.

Fig. 3 shows the dependence of the cohesive zone conductance on the normal displacement jump for the case of $\psi = 0^\circ$. In Fig. 3(a) values of the cohesive zone conductance are given for heat transfer across the cohesive zone due to the presence of fibers only. Corresponding data for the volume fraction of fibers in the crack as well as for the survival probability are depicted. Initially for small values of Δ_n , the bridging fibers do not contribute much to h_{CZ} since their orientation is perpendicular to the heat flux. The initial value of h_{CZ} can be calculated from Eq. (30) as $h_{CZ} = h_f = 0.0954$ $\text{MW/m}^2\text{K}$. This value of h_{CZ} remains nearly constant until the displacement jump increases to $\Delta_n = 0.5$ μm . As the displacement jump increases, the fiber bridging angle starts to increase such that surviving fibers can contribute more to h_{CZ} . Nevertheless, due to the simultaneously occurring decay of V_f^C the contribution of fibers actually drops with increasing opening. The cohesive zone conductance decreases, and for $\Delta_n > 70$ μm is reduced to very small values. The value of displacement jump at which the conductance drops to near zero can be identified as the thermal cohesive length. Fig. 3(a) also compares the values for the case of $h_{CZ} = h_f$ to those for the case with a crack containing air (1 atm.), only, ($h_{CZ} = h_g$). In this case h_{CZ}

follows $1/\Delta_n$. As fibers are mostly aligned perpendicular to the heat flux $h_g > h_f$. Model prediction compare favorable with the trends in the experimental study of McDonald et al. (2000).

To obtain a more complete picture of the conductance properties the case of a cohesive zone accounting for fibers, air (1 atm.) entrapped in the crack and radiation is considered. The contribution of h_g , h_f and h_r to the total conductance, h_{CZ} , are given in Fig. 3(b). In the presence of both air and bridging fibers, the initial conductance is dominated by h_g and h_f weighted by the volume fraction of fiber, V_f^C . With the maximum value of V_f^C , h_{CZ} in this case is obtained as $0.17 \text{ MW/m}^2\text{K}$. This value is less than that for a cohesive zone with air only, as some volume in the crack is occupied with fiber perpendicular to the heat flux. Consequently, the contribution of the conductance due to gas, h_g , is the main contribution to the cohesive zone conductance for most of the range of Δ_n . Only at large values of Δ_n , as all fibers have failed and the conductance through air has vanished due to the large separation, the contribution of radiation, h_r , becomes noticeable. This contribution to the cohesive zone conductance is small for the temperatures considered, i.e. $\max(h_r) = 1 \times 10^{-4} \text{ MW/m}^2\text{K}$.

The cohesive zone conductance in dependence of Δ_n under mixed mode loading conditions is shown in Fig. 3(c). For the case of a cohesive zone with fiber in vacuum an increase in mode mixity leads to a faster decrease in h_{CZ} . The thermal cohesive length for $\psi \rightarrow 90^\circ$ is considerably smaller than for $\psi = 0^\circ$, i.e. only $3.7 \mu\text{m}$. However, for a cohesive zone containing air there is essentially no change in the cohesive zone conductance with mode mixity. At 1 atm. air provides the dominating factor in heat transfer, and this contribution is independent of ψ and only depends on Δ_n .

4. Laminate with a bridged crack

4.1. Geometry and boundary conditions

Numerical studies are carried out for a laminates of thickness $H = 2 \text{ mm}$ and length $L = 30 \text{ mm}$, Fig. 4(a). Bridged cracks of fixed length $2a$ are positioned at $H_1 = 0.211H$ from the upper hot laminate surface. This location of the crack provides the maximum value of energy release rate in specimen loaded by a temperature gradient and traction free boundary conditions (Hutchinson and Lu, 1995). The lengths for the bridged delamination cracks are considered between $a/H = 2.0$ and 6.0 .

Initially the laminates are at the reference temperature $\theta_0 = 300 \text{ K}$. A temperature change linearly increasing in time is applied to the top surface, $[y = H]$, with the maximum temperature reaching $\max(\theta_{\text{top}}) = 1500 \text{ K}$. The temperature at the bottom, $[y = 0]$, is kept constant at the initial temperature $\theta_{\text{bot}} = \theta_0$. The sides $[x = \pm L]$ are insulated. The displacement boundary conditions considered are those of traction free laminates. The boundary conditions applied are $u_y[(x = 0), (y = 0)] = 0$. Coupled temperature–displacement solutions in steady state are computed for a half models of the laminates with the symmetry plane at $[x/a = 0]$.

The finite element model is shown in Fig. 4(b). The length of the cohesive elements was chosen to be $50 \mu\text{m}$, smaller than the cohesive lengths expected.

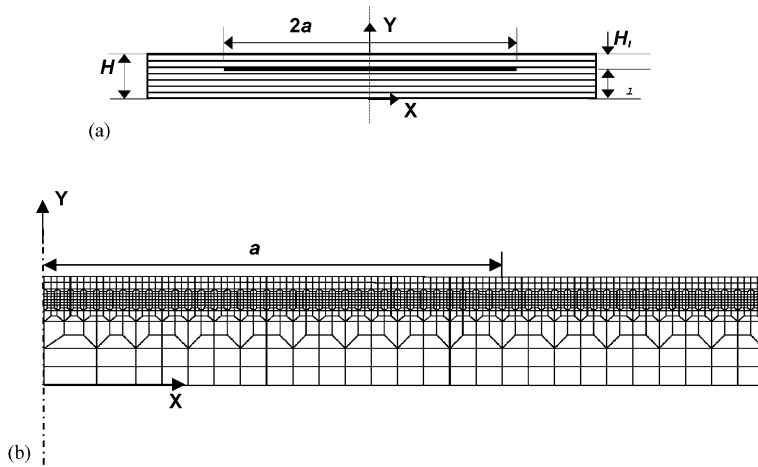


Fig. 4. (a) Specimen geometry and (b) finite element mesh.

Continuum elements used in the finite element model are four node plane strain temperature–displacement elements. A frictionless contact condition is employed at the crack surfaces. In contact, the thermal resistance of the cohesive zone is continuous to the thermal resistance during opening. Radiative heat transfer between the crack surfaces is accounted for in all simulations. The analysis of the laminates with buckling was facilitated by use of the STABILIZE option in ABAQUS. This introduces pseudo-damping proportional to the displacement velocity of the nodes, thus leading to a pseudo time integration of the buckling response. Default values provided in ABAQUS were reduced as much as possible to provide smallest impact on the analysis results.

Values for the total energy release rate, G_T , are obtained by use of the modified crack closure integral (Venkatesha et al., 1996), with its components G_I and G_{II} being computed from nodal forces and displacements at the crack tip.

4.2. Results

4.2.1. Bending deformation

As the applied temperature difference between the top and bottom of the laminate, $\theta_{\text{top}} - \theta_{\text{bot}}$, increases the thermal expansion differences lead to bending of the specimens. Contour plots of temperatures on the deformed specimen configurations are depicted in Fig. 5 for $a/H = 2.0$ at four values of applied temperature difference. The cohesive zone represents a bridged delamination crack containing air at 1 atm., see Table 3. As the applied temperature difference across the laminate is increased, bending of the laminate opens the crack and induces a disturbance into the temperature field. The details of the thermomechanical bridging behavior will determine the temperature distribution and thus the loading of the crack.



Fig. 5. Temperature contour plots for a laminate $a/H = 2.0$ at applied temperature difference, $\theta_{\text{top}} - \theta_{\text{bot}}$: (a) 300 K, (b) 600 K, (c) 900 K and (d) 1200 K.

Table 3

Parameter values for the cohesive zone model

Initial bridging span, l_0 [μm]	200.0
Fiber diameter, d [μm]	15.0
Interface shear resistance, τ [MPa]	15.0
Matrix fracture toughness, K_{IC}^m [MPa $\text{m}^{1/2}$]	3.0
Weibull modulus of fiber, m	3.1
Weibull reference length, l_{ref} [mm]	25.0
Weibull reference strength, σ_{ref} [GPa]	1.63
Number of fibers/fracture surface area, n_0 [mm^{-2}]	14.0
Thermal conductivity of gas (air), k_g [W/mK]	0.032–0.1 (300–1500 K)

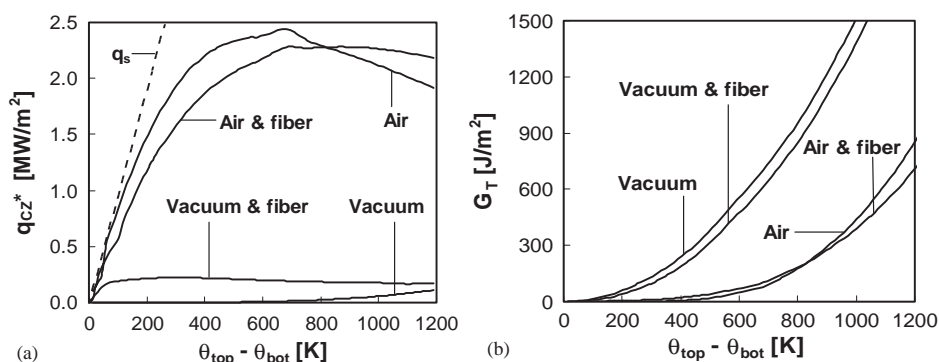


Fig. 6. Predicted values of (a) q_{CZ}^* , (b) G_{T} in dependence of the applied temperature difference for $a/H = 2.0$ and different crack environments.

In Fig. 6, the influence of different crack environments is shown for the crack length $a/H = 2$ and four different crack conditions: vacuum, vacuum with bridging fibers, air at 1 atm., and air (1 atm.) with bridging fibers. Computed values of q_{CZ}^* , the heat flux across the crack at $x/a = 0.0$, are depicted in Fig. 6(a), and compared to the

heat flux across an uncracked laminate, $q_s = -k_T d\theta/dy$, with k_T the transverse thermal conductivity of the composite. For the case of the crack with vacuum, the crack is virtually insulating except at high temperatures where radiation becomes noticeable. For the laminate with bridging fibers in vacuum only a small increase in the conductance is observed relative to the pure vacuum case as the bridging fibers are nearly perpendicular to the temperature gradient. In the presence of gas in the crack, the crack heat flux is considerably increased. At low temperature differences, the heat flux across the cracks containing gas does not deviate significantly from the Fourier law of the undisturbed solid, q_s . With air only, the crack heat flux reaches its peak of 2.4 MW/m^2 at a temperature difference of 700 K. Subsequently, q_{CZ}^* drops as the opening of the crack increases. As fibers are added, lower heat flux values are seen initially as the fibers perpendicular to the temperature gradient provide insulating action. Nevertheless, the presence of bridging fibers reduces the crack opening, thus the heat flux reaches its peak value at a higher applied temperature difference (850 K) and no significant drop in q_{CZ}^* is observed after that.

Fig. 6(b) depicts the energy release rate, G_T , in dependence of the applied temperature difference. The largest amount of mechanical loading occurs for the crack under vacuum. In the presence of bridging fibers the crack opening is slightly restraint and crack shielding reduces G_T . Considerable lower values of G_T are present if gas is present in the crack. Lower values of the temperature difference across the crack keep the crack closed until a temperature difference of 300 K, and lead to considerably reduced values of G_T even for the open crack. The addition of bridging fibers in the crack only provides a small further reduction of G_T further inhibiting crack opening as higher values of the applied temperature difference are reached.

The current computational results differ in an important features from the results on the energy release rate obtained in Hutchinson and Lu (1995). There, results for thermal gradient loading of a laminate without crack bridging were determined under the assumptions of a constant crack opening displacement along the crack, and a correlation between crack face separation and energy release rate based on a solution for a crack in an infinite medium was used. A marked threshold in the applied temperature difference was predicted below which the energy release rate remained zero. In contrast, in the present analysis the displacement jump across the crack and thus the heat flux across the crack depend on location. Consequently, in the present finite-element results thresholds in the dependence of the G_T on the applied temperature difference are not as clearly present.

4.2.2. Transition from bending to buckling

In this section the effects of crack length on the failure mechanisms of the laminates are discussed. Results for delamination cracks of lengths $a/H = 2.0, 3.0, 3.5, 4.0$ and 6.0 are presented for the case that cracks are fully bridged by fibers, contain air (1 atm.). Fig. 7(a) shows computed values of q_{CZ}^* . For all crack lengths, a large fraction of the conductance of the undisturbed laminate is recovered initially. Only for $a/H = 2.0$ the heat flux across the crack does not break down such that large values of q_{CZ}^* can be sustained over the full range of applied temperature differences considered. For longer cracks initial values of q_{CZ}^* are also close to q_s , but the maximum values of q_{CZ}^* become

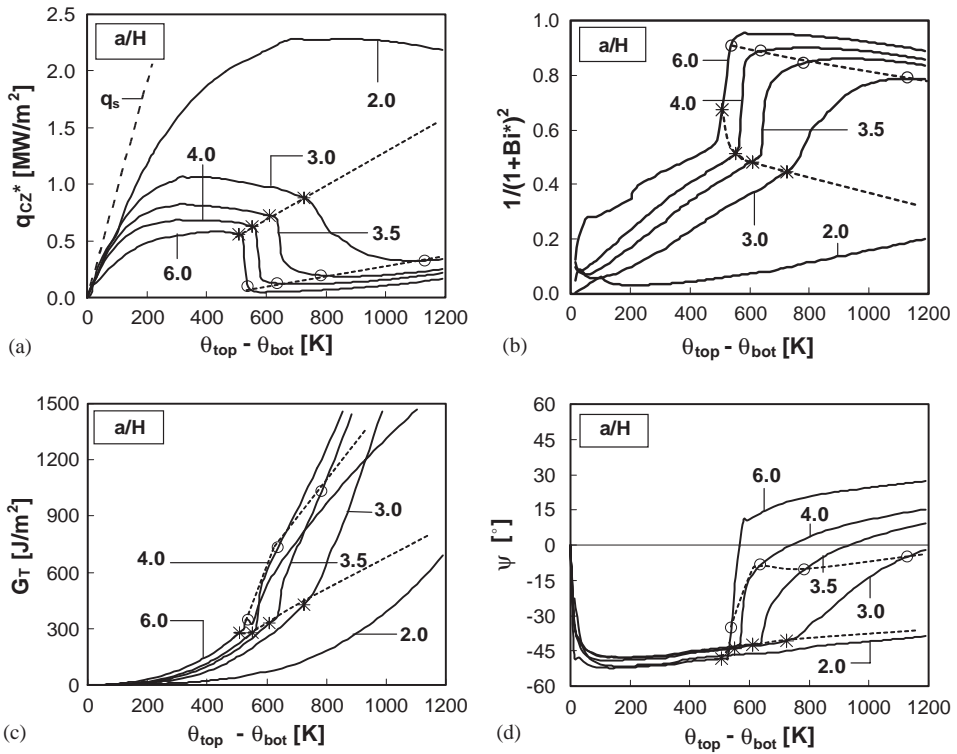


Fig. 7. Predicted values of (a) q_{CZ}^* , (b) $1/(1+Bi^*)^2$, (c) G_T and (d) ψ in dependence of the applied temperature difference for various crack lengths a/H . All cracks with air, bridging fibers and radiation.

significantly smaller with increasing crack length. For $a/H = 6.0$ the maximum value of q_{CZ}^* is 0.58 MW/m^2 , i.e. only one fourth of the value found for $a/H = 2.0$. For cracks with $a/H \geq 3.0$ heat flux across the crack breaks down as the applied temperature differences reach 725, 609, 551 and 507 K for $a/H = 3.0, 3.5, 4.0, 6.0$, respectively. For larger values of the applied temperature, $q_{CZ}^* \simeq h_r \Delta\theta$.

In Fig. 7(b), the heat flux across the crack is characterized by use of the Biot number, $Bi^* = (h_{CZ}H)/k_T$, at $x/a = 0.0$. Following Lu and Hutchinson (1995) the energy release rate scales with $1/(1+Bi^*)^2$. For the short crack ($a/H = 2.0$), $1/(1+Bi^*)^2$ remains close to zero indicating a nearly perfectly conducting crack with $Bi = \infty$. For long delamination crack lengths $1/(1+Bi^*)^2$ transitions from zero to one, indicating an nearly insulating crack at large values of applied temperature difference with $Bi = 0$. The transition from a conducting to an insulating crack occurs in three stages, the first one corresponding to a reduction in Bi^* under increasing q_{CZ}^* . Subsequently, a strong reduction in Bi^* occurs as q_{CZ}^* drops to a value dominated by radiation. Break down in q_{CZ}^* and onset of the strong drop in Bi^* coincides well with the condition that the volume fraction of fibers in the crack reaches a low level, $V_f^C = 0.01$ at $x/a = 0.0$. This condition of breakdown in thermal shielding is marked by a (*) in the curves in

Fig. 7, as well as in subsequent figures. As should be recalled from Fig. 3, a drop in $V_f^C = 0.01$ for the current material is in general achieved due to a large crack opening, with the fiber survival probability still remaining high. During the drop in q_{CZ}^* the fiber survival probability drops sharply. The condition of breakdown of mechanical shielding at $p_s = 0.1$ at $x/a = 0.0$ as marked by (\circ) in the plots. This condition also indicates the onset of the radiation dominated thermal regime. For a crack with $a/H = 3.0$ the applied temperature difference between these two points is large, while for $a/H = 6.0$ both events occur closely together.

Based on the results for the Biot number, the predicted values of the energy release rate and the mode mixity are expected to be considerably dependent on the crack length, Fig. 6(c–d). For the shortest cracks, $a/H = 2.0$, a continuous increase in G_T with applied temperature difference is observed together with a nearly constant mode mixity of approximately -45°C . Both the thermal and the mechanical bridging remain intact. For the longer crack lengths a distinct change in slope of the G_T curve is present. For the first part of loading, bending dominates and the mode mixity is similar to that for the short crack. In the bending regime the computed values of G_T depend only on the crack length as a steady state is reached with increasing a/H .

As the heat flux across the crack breaks down and the crack becomes insulating, a buckling delamination is formed and the rate of increase in G_T rises substantially. The transition from bending to buckling deformation is clearly seen from the results of the crack tip mode mixity. At the breakdown of crack heat flux, the mode mixity changes sign and subsequently is dominated by the opening component. For $a/H = 3.0$ this transition still occurs gradually over a significant applied temperature difference interval, while for long cracks an instantaneous change is present. During this process the normal displacement jump, Δ_n at $x/a = 0.0$ increases significantly, $\Delta_n = 750\ \mu\text{m}$ for $a/H = 6.0$, and $\Delta_n = 80\ \mu\text{m}$ for $a/H = 3.0$. For the buckled laminates, the values of energy release rate and mode mixity now are dependent on crack length. In the buckled state crack tip shielding remains effective only for the crack with $a/H = 3.0$ but vanishes already during the buckling process for long cracks.

Two contour lines (connecting $V_f^C = 0.01$ and $p_s = 0.1$, respectively) are included in Fig. 7 indicating regimes of loading and crack lengths that allow for the specimen to sustain the thermal loading without a breakdown in thermal and mechanical bridging, respectively. As thermal crack bridging in the presence of a gas is essentially driven by the normal displacement jump a breakdown in thermal bridging is essentially reversible. This is, however, not the case for the mechanical bridging. As $p_s = 0.1$ is crossed, all mechanical bridging is lost.

4.2.3. Pronounced buckling

The influence of different crack environments in the case of pronounced buckling is documented for the crack length of $a/H = 4$. Fig. 8 depicts contour plots of the temperature distribution on the deformed specimen configuration for a bridged delamination cracks containing air (1 atm.). Initially, the delamination crack is nearly closed, and the crack presents only a small disturbance to the temperature field, such that the overall deformation mode is again in bending, Figs. 8(a–b). At the critical temperature difference, the crack opens rapidly and the formation of the buckling delamination is

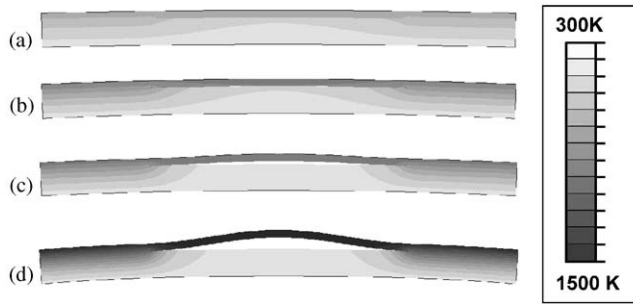


Fig. 8. Temperature contour plots for a laminate $a/H = 4.0$ at applied temperature difference, $\theta_{\text{top}} - \theta_{\text{bot}}$: (a) 300 K, (b) 540 K, (c) 600 K and (d) 1200 K.

seen clearly, Fig. 8(c). As a consequence the temperature jump across the crack increases and finally the crack becomes fully insulating such that the temperature jump across the crack is identical to the applied temperature difference, Fig. 8(d).

The details of the thermal response for $a/H = 4.0$ and four different crack environments are depicted via q_{CZ}^* and $1/(1 + Bi^*)^2$ in Figs. 9(a) and (b). The conditions $V_f^C = 0.01$ and $p_s = 0.1$ are identified. With vacuum the crack is virtually insulating except at high temperatures where radiation becomes noticeable. For the laminate with bridging fibers in vacuum, again only a small increase in the conductance is observed. For specimens with cracks containing air at 1 atm., the conductance is considerably increased and is initially close to that of the uncracked laminate. In the case of a crack containing air only, the initially large values of q_{CZ}^* are sustained up to small values of applied temperature difference only, and q_{CZ}^* breaks down already at 131 K. As crack bridging is absent, the crack opening occurs without any restraints. For the crack containing air and fibers, the most favorable picture emerges. The bridging fibers keep the crack closed such that air remains effective in transporting heat across the crack and thus delay the onset of the buckling delamination. A heat flux across the crack is sustained to considerably higher values of applied temperature difference, i.e. $\theta_{\text{top}} - \theta_{\text{bot}} = 507$ K. After buckling, in the presence of gas, q_{CZ}^* remains above that for the crack with vacuum even at large values of applied temperature difference. Values of $1/(1 + Bi^*)^2$ are given in Fig. 9(b). For the crack with vacuum $1/(1 + Bi^*)^2$ is equal to one except for high values of applied temperature differences where radiation starts to contribute to crack conductance. For the other cases, however, $1/(1 + Bi^*)^2$ approaches zero at different values of applied temperature difference with the effect of crack bridging is again clearly visible. For bridged cracks the Biot number remains at large values up to considerably larger temperature differences than for the unbridged cracks indicating lower values of crack tip loading for these cases.

Computed values of energy release rate and mode mixity are depicted in Figs. 9(c) and (d), respectively. For the crack with vacuum, due to the strongly insulating effect of the crack, the values of G_T are non-zero already for small values of applied temperature difference, and increases steadily with an increase in $\theta_{\text{top}} - \theta_{\text{bot}}$. As fibers are included in the crack, the computed value of G_T are slightly smaller than for the perfectly

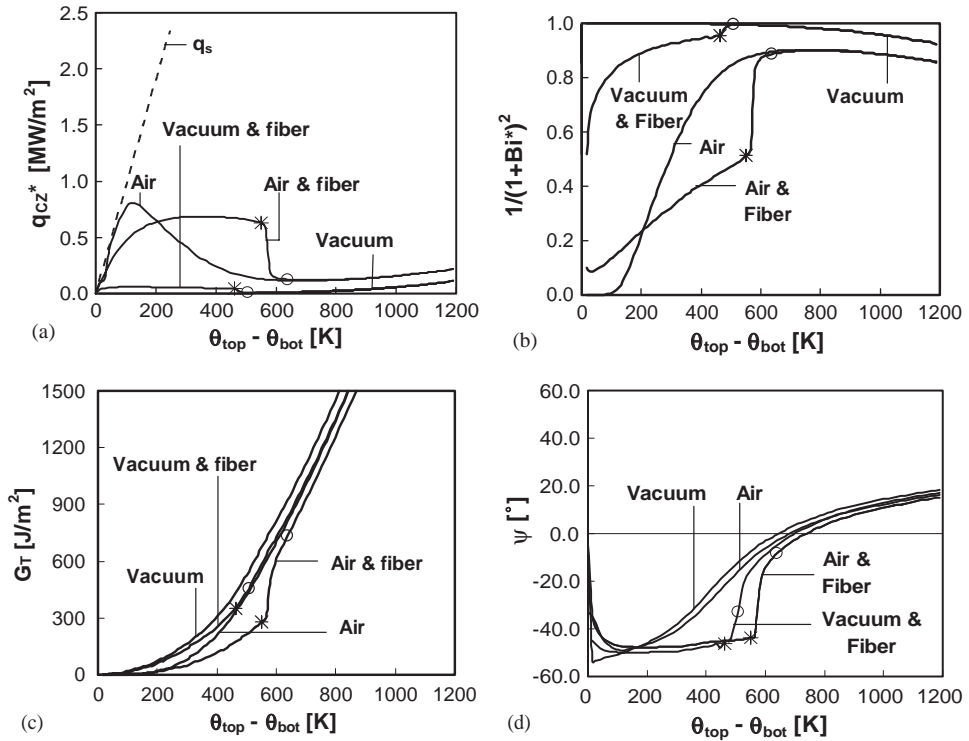


Fig. 9. Predicted values of (a) q_{CZ}^* , (b) $1/(1+Bi)^2$, (c) G_T and (d) ψ in dependence of the applied temperature difference for $a/H = 4.0$ and different crack environments.

insulating crack due to the mechanical and thermal shielding effects. The action of the bridging fibers in delaying the onset of the formation of the buckling delamination is seen clearly in the mode mixity values. For a crack filled with air, but without bridging fibers, G_T initially remains low as only a low level of thermal stresses are being induced by the conducting crack. However, due to the early break-down in conductance G_T rises rapidly soon. As bridging fibers are added the values of G_T are reduced and remain at low levels for values of the applied temperature difference up to 507 K as a consequence of mechanical and thermal shielding. As $V_f^C = 0.01$ is reached at $x/a = 0$, a pronounced change in the dependence of G_T on $\theta_{\text{top}} - \theta_{\text{bot}}$ occurs. Related to the break down in q_{CZ}^* , the value of $dG_T/d(\theta_{\text{top}} - \theta_{\text{bot}})$ increases at this temperature difference due to the reduction in crack heat flux due to higher level of the resulting thermal stresses. Still, the mechanical action of crack bridging remains effective and keeps G_T to the lowest level for all four cases considered in Fig. 8(c).

The computed values of the mode mixity are given in Fig. 9(d) in dependence on the applied temperature difference. For applied temperature differences below the breakdown of crack heat transfer the mode mixity is constant for the cracks with bridging fibers, $\psi = -47^\circ$. As the crack conductance starts to break down, the mode

mixity starts to increase, then becomes positive at the onset of bridging breakdown, and finally reaches $\psi = 20^\circ$. For the cracks without crack bridging the initial and final values of the mode mixity are the same. The presence of bridging fibers delays the onset of buckling and leads to a much sharper transition from the bending into the buckled mode.

4.3. Parametric study on crack bridging parameters

The thermomechanical cohesive zone model is based on the micro-mechanism of the crack bridging processes with the mechanical and thermal response of the cohesive zone as the outcome of the boundary value problem. Consequently, the present cohesive model approach can be used to directly assess the influence of the microlevel crack bridging parameters on the macroscopic specimen response. In terms of material design, this allows to identify material parameters important for a specific loading configuration. A parametric study is carried out in order to demonstrate the effect of different types of cohesive zone parameters on the response of the cracked laminate under thermomechanical loading. The bridging parameters investigated here are divided into three categories. Cohesive zone parameters dominantly affecting the thermal cohesive zone behavior are accounted for in terms of variations in the gas conductivity. Mechanical cohesive zone properties are represented by the fiber reference strength, σ_{ref} , and the interface sliding stress, τ . These values of these parameters can change due to the presence of manufacturing conditions or environmental degradation. Parameters affecting both the thermal as well as the mechanical behavior of the cohesive zone are representative of changes in the composite microstructure. As the fiber misalignment in the nominally unidirectional reinforced laminate changes, the number of bridging fibers per crack surface area left behind by the matrix crack, n_0 , as well as the length of the bridging fiber segments, l_0 , change. Results in the parametric study stem from computations for laminates with $a/H = 4.0$. The cohesive zone represents conductance through the available fibers and air, respectively, as well as radiative heat transfer.

From the results in the previous sections it is evident that the influence of the thermal parameters of the response of the delamination crack to the temperature gradient can be significant. The contribution of gas entrapped in the crack emerges as an important contribution to the crack conductance and thus strongly determines the actual loading. In actual applications, the contribution of gas to the conductance across the crack can change with chemical composition of the gas, the ambient gas pressures as well as with the diffusion of gas into the delamination crack, (Mogro-Campero et al., 1997). Four values of gas conductivity were considered ($0.25k_g, 0.5k_g, k_g, 2.0k_g$) in addition to a crack with no gas. Fig. 10(a) and (b) depict q_{CZ}^* and G_{T} , respectively. Increased gas conductance increases the heat flux across the crack and reduces the mechanical loading of the crack. Thereby, the temperature difference needed for the onset of the breakdown in heat flux is shifted to higher values. The results show that an increase of k_g is an effective means to increase the structural integrity of the laminates. Increasing k_g reduces the level of G_{T} and increases the critical temperature difference needed for the onset of buckling delamination. While bending causes the crack to open for all k_g

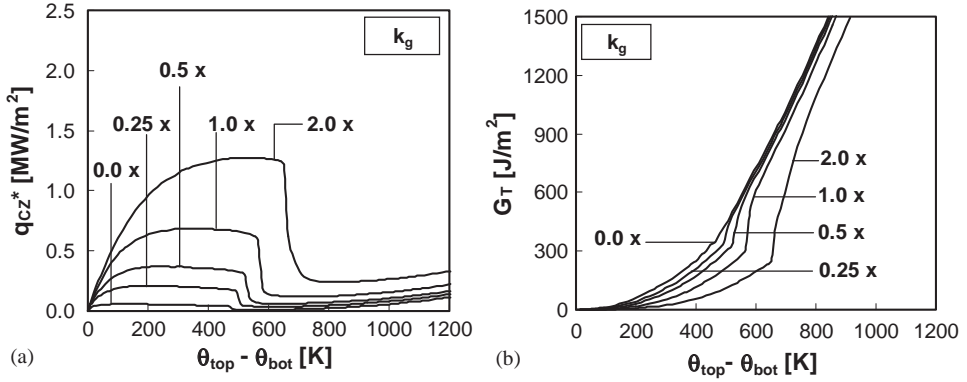


Fig. 10. Influence of gas conductance, k_g , on predicted values of (a) cohesive zone heat flux ($x/a=0.0$) and (b) G_T in dependence of the applied temperature difference.

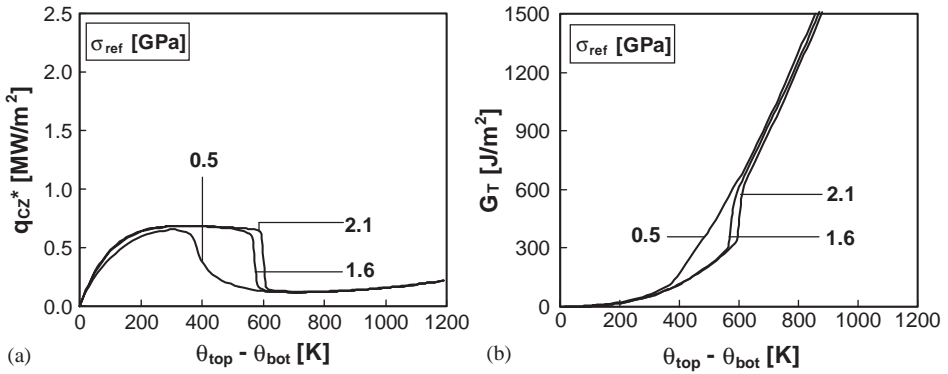


Fig. 11. Influence of fiber strength, σ_{ref} , on predicted values of (a) q_{cz}^* and (b) G_T in dependence of the applied temperature difference, $a/H = 4.0$.

values, higher values of k_g extend the bending regime and delay buckling, e.g. for a crack containing gas of conductivity 25% of that of air at 1 atm. buckling to occurs at $\theta_{top} - \theta_{bot} = 480$ K, while for a crack containing a gas of conductivity twice that of air at 1 atm. Buckling is delayed until $\theta_{top} - \theta_{bot} = 653$ K.

Changes in the fiber reference strength, σ_{ref} , lead to changes in the cohesive strength but leave the initial stiffness of the traction–separation response unchanged. The heat flux at the crack center for the bridged crack and the values for G_T are depicted in Fig. 11 for reference strengths of $\sigma_{ref} = 0.5, 1.6$ and 2.1 GPa, respectively. As fiber strength is changed virtually no changes in the initial heat flux values and the maximum heat flux across the delamination crack is predicted. The only impact on q_{CZ}^* is that the breakdown in heat flux depends on the fiber strength. While the breakdown temperature difference increases by approximately 200 K as σ_{ref} increases from 0.5 to 1.6 GPa, a

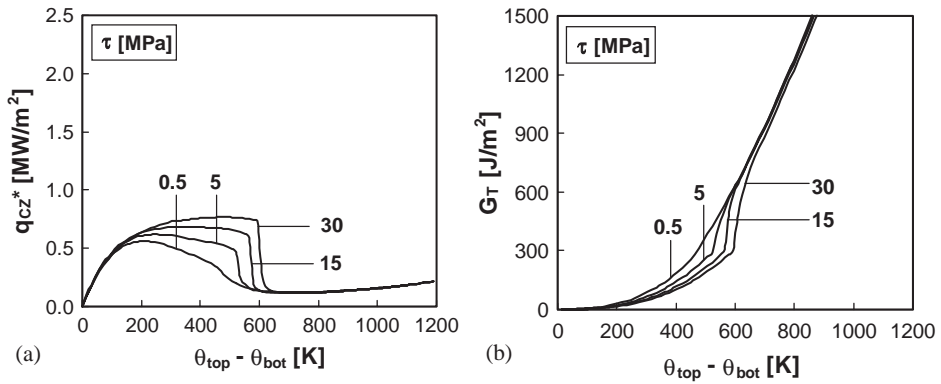


Fig. 12. Influence of fiber–matrix interface sliding stress, τ , on predicted values of (a) q_{CZ}^* and (b) G_T in dependence of the applied temperature difference, $a/H = 4.0$.

further increase to 2.1 has less additional effect. However, higher values of σ_{ref} lead to a more pronounced formation of the buckling delamination of the specimen.

Matrix–fiber interface properties are represented by the interface sliding stress. A variation in this parameter changes the initial stiffness of the traction separation response but keeps the cohesive strength the same. Computed values of q_{CZ}^* and G_T are shown in Fig. 12(a) and (b) for values of τ between 0.5 to 30 MPa. Low values of τ allow for larger values of crack opening early on leading to reduced values of q_{CZ}^* and larger values of G_T . An increase in τ restrains the opening of the crack and leads to the formation of a pronounced buckling delamination ($\theta_{top} - \theta_{bot} = 510$ K for $\tau = 5$ MPa, increasing to $\theta_{top} - \theta_{bot} = 600$ K for $\tau = 30$ MPa). The present observation that an increase in the stiffness of the bridging zone delays the onset of buckling is consistent with recent findings in a study on the stability of sandwich structures with compliant interfaces, Volokh and Needleman (2002).

Predictions for four different values of the initial spanning length, l_0 , are given in Fig. 13. A decrease in the initial spanning length increases the initial stiffness of the traction–separation response, increases the cohesive strength and the fiber bridging angle φ , and changes the thermal response by decreasing the volume fraction of fibers in the crack, V_f^C . As l_0 is decreased from 300 to 50 μm , the crack conductance increases considerably despite the reduction in V_f^C . This behavior can be contributed to increased bridging angles for short spanning lengths, as well as the reduced amount of crack opening due to the increased stiffness of the traction–separation response. Furthermore, the increase in cohesive strength with smaller l_0 values explains the delay in the onset of buckling delamination with reduced l_0 . The resulting larger heat flux values lead to smaller thermal stresses, and lower values of G_T during the bending dominated region and a delay in the onset of the buckling delamination.

Fig. 14 depicts results considering the variation in the number of bridging fibers per crack surface area with n_0 ranging from 0 to 28 fibers per mm^2 . An increase in n_0 increases the initial stiffness of the traction–separation response, leads to a

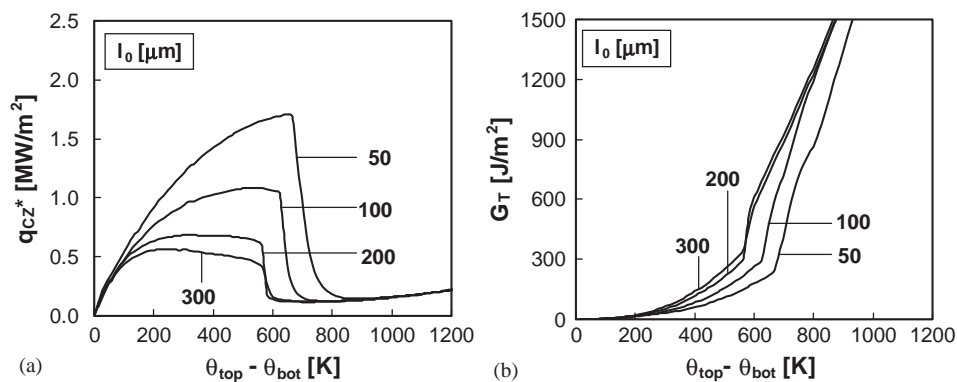


Fig. 13. Influence of initial fiber bridging length, l_0 , on predicted values of (a) q_{CZ}^* and (b) G_T in dependence of the applied temperature difference, $a/H = 4.0$.

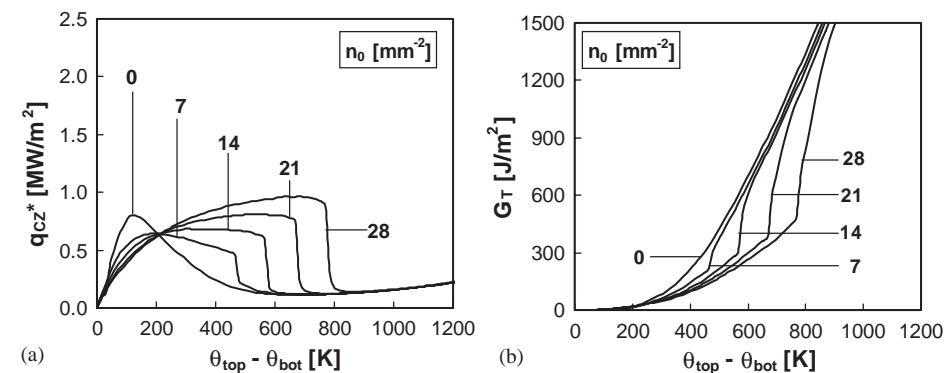


Fig. 14. Influence of the number of bridging fibers per crack surface area, n_0 , on predicted values of (a) q_{CZ}^* and (b) G_T in dependence of the applied temperature difference, $a/H = 4.0$.

higher cohesive strength, and increases the volume fraction of fibers in the crack. These effects are beneficial to specimens as they restrict the opening of the crack and enhance conduction across the crack. While an increase in n_0 influences the peak values of heat flux across the delamination crack only slightly, it strongly changes the value of applied temperature difference to break down of conductance. Consequently, for different values of n_0 the main impact of an increase in n_0 is a shift of breakdown of q_{CZ}^* to significantly higher applied temperature differences. The higher stiffness of the traction–separation law reduces the energy release rate in the bending mode while a higher cohesive strength delays the onset of delamination buckling.

5. Summary

A framework for investigations of composite laminates with bridged delamination cracks under thermomechanical loading has been established. A micro-mechanism based thermomechanical cohesive zone model has been formulated for use in this analysis. In this approach both the traction–separation as well as the crack conductance–separation behavior is the outcome of the constitutive cohesive zone formulation. The coupled thermomechanical CZM reasonably captures the features found in studies on delamination crack growth as well as in experiments on the heat conductance across delamination cracks.

The thermomechanical cohesive zone model is applied to a study of the mechanics of bridged cracks in a ceramic matrix laminate subjected to an applied temperature difference across the laminate. Coupling between stress analysis and heat transfer analysis occurs not only due to thermal stresses, but also due to the changes in load transfer and thermal conductance across the delamination crack.

Two length scale parameters are present in the thermomechanical cohesive zone model, a mechanical and a thermal cohesive length. These parameters are dependent on the micromechanisms of failure and heat transfer across the crack, and can be dependent on the mode mixity. The mechanical cohesive length values are related primarily to the survival probability of bridging fibers. The mode mixity dependence of the mechanical cohesive length emerges as the outcome of the competition between matrix spalling and fiber pull-out. For the thermal cohesive length the interactions between the bridging fibers and a gas in the crack play a significant role. If the contribution of the gas to the crack conductance dominates over the conductance provided by the bridging fibers, then the crack conductance is depends inversely on the normal material separation and is independent of the mode mixity. For cracks without a dominant contribution from a gas but with bridging fibers, the crack conductance is related to the volume fraction of bridging fibers in the crack. This quantity depends linearly on the survival probability and inversely on the normal separation. For a crack without dominant gas contribution, the thermal cohesive zone length is thus smaller than the corresponding mechanical cohesive zone length and dependent on the mode mixity. For the cohesive zone parameters selected in the present study, the breakdown of heat transfer across the crack precedes the breakdown of the load transfer across the delamination crack.

Crack bridging influences the specimen response to thermal gradient loading in several aspects. It decreases the amount of crack opening, and allows for a less disturbed heat flux across the crack. This in turn leads to reduced thermal stresses. As a result, the energy release rate at the crack tip is reduced, and the critical temperature difference for the onset of buckling delamination is increased. The specific details of the crack environment strongly affect the response to the applied temperature gradient. The contribution of gas entrapped in the delamination crack emerges as a major contribution to the conductance of the crack. Nevertheless, gas remains an effective conductor in the crack only as long as the crack opening is small which can be achieved due to the presence of bridging fibers. Material parameters for the bridging zone influencing the initial stiffness of the traction–separation response are effective mainly in reducing the energy release rate in the bending regime. Changes in the resulting cohesive

strength mainly delay the onset of the buckling delamination. The present thermomechanical cohesive zone model emerges as a versatile tool in these simulations as it allows one to directly determine the influence of micro-level bridging parameters on the overall structural response of the specimen.

Computed values of G_T are well above the toughness of the matrix of the composite under investigation such that further growth of the delamination cracks is to be expected. Then, with increasing crack length, the onset of buckling delamination is likely. Computations in which the growth of the matrix crack is accounted for in competition with the build-up and breakdown of fiber bridging remain to be conducted.

Acknowledgements

The financial support from Sandia National Laboratories through the NSF-Sandia Life Cycle Engineering Program is gratefully acknowledged.

Appendix A. Nodal shape functions

$$\mathbf{N}_m = \begin{bmatrix} \frac{1+\xi}{2} & \frac{1-\xi}{2} \\ \frac{1-\xi}{2} & \frac{1+\xi}{2} \end{bmatrix}, \quad \mathbf{N}_{tm} = \begin{bmatrix} 1 & 0 \\ 0 & 1 \end{bmatrix}, \quad N_{th} = \begin{bmatrix} 1 \\ 0 \end{bmatrix}. \quad (\text{A.1})$$

Appendix B. Derivatives of the traction–separation model

The derivatives of the tractions, $\mathbf{T}_{CZ}(\Delta)$, with respect to normal Δ_n and tangential displacement jump Δ_t , present in the Jacobian, \mathbf{J}_m , can be expressed as

$$\frac{\partial T_n}{\partial \Delta_n} = n(\Delta) \frac{\pi d^2}{4} \left[\frac{\sigma_p(\Delta)}{l_0 + \Delta_t} + \frac{\partial \sigma_p(\Delta)}{\partial \Delta_n} \tan \varphi \right] + \frac{\partial n(\Delta)}{\partial \Delta_n} f_n(\Delta), \quad (\text{B.1})$$

$$\frac{\partial T_n}{\partial \Delta_t} = n(\Delta) \frac{\pi d^2}{4} \left[-\sigma_p(\Delta) \frac{\Delta_n}{(l_0 + \Delta_t)^2} + \frac{\partial \sigma_p(\Delta)}{\partial \Delta_t} \tan \varphi \right] + \frac{\partial n(\Delta)}{\partial \Delta_t} f_n(\Delta), \quad (\text{B.2})$$

$$\frac{\partial T_t}{\partial \Delta_n} = \frac{1}{2} \left[n(\Delta) \frac{\pi d^2}{4} \frac{\partial \sigma_p(\Delta)}{\partial \Delta_n} + \frac{\partial n(\Delta)}{\partial \Delta_n} f_t(\Delta) \right], \quad (\text{B.3})$$

$$\frac{\partial T_t}{\partial \Delta_t} = \frac{1}{2} \left[n(\Delta) \frac{\pi d^2}{4} \frac{\partial \sigma_p(\Delta)}{\partial \Delta_t} + \frac{\partial n(\Delta)}{\partial \Delta_t} f_t(\Delta) \right]. \quad (\text{B.4})$$

The derivatives of the number of surviving fibers, $n(\Delta)$, with respect to displacement jump are,

$$\frac{\partial n(\Delta)}{\partial \Delta_n} = n_0 \exp \left[-C_b \frac{l(\Delta)}{l_{\text{ref}}} \left(\frac{\bar{\sigma}(\Delta)}{\sigma_{\text{ref}}} \right)^m \right] \left[-m C_b \frac{l(\Delta)}{l_{\text{ref}}} \left(\frac{\bar{\sigma}(\Delta)}{\sigma_{\text{ref}}} \right)^{m-1} \frac{\partial \bar{\sigma}(\Delta)}{\partial \Delta_n} - \frac{C_b \Delta_n}{l_{\text{ref}} l(\Delta)} \left(\frac{\bar{\sigma}(\Delta)}{\sigma_{\text{ref}}} \right)^m \right], \quad (\text{B.5})$$

$$\frac{\partial n(\Delta)}{\partial \Delta_t} = n_0 \exp \left[-C_b \frac{l(\Delta)}{l_{\text{ref}}} \left(\frac{\bar{\sigma}(\Delta)}{\sigma_{\text{ref}}} \right)^m \right] \left[-m C_b \frac{l(\Delta)}{l_{\text{ref}}} \left(\frac{\bar{\sigma}(\Delta)}{\sigma_{\text{ref}}} \right)^{m-1} \frac{\partial \bar{\sigma}(\Delta)}{\partial \Delta_t} - \frac{C_b (l_0 + \Delta_t)}{l_{\text{ref}} l(\Delta)} \left(\frac{\bar{\sigma}(\Delta)}{\sigma_{\text{ref}}} \right)^m \right]. \quad (\text{B.6})$$

The derivatives of combined fiber stress, $\bar{\sigma}(\Delta)$, with respect to displacement jump are,

$$\begin{aligned} \frac{\partial \bar{\sigma}(\Delta)}{\partial \Delta_n} &= \frac{\partial \sigma_p(\Delta)}{\partial \Delta_n} + \frac{\partial \sigma_b(\Delta)}{\partial \Delta_t} \\ &= \sqrt{\frac{\tau E_f \Delta_n^2}{\left[\sqrt{(l_0 + \Delta_t)^2 + (\Delta_n)^2} - l \right] [(l_0 + \Delta_t)^2 + (\Delta_n)^2] d}} + \frac{E_f}{\delta/d} \left[\frac{\Delta_n}{(l_0 + \Delta_t)^2} \right], \end{aligned} \quad (\text{B.7})$$

$$\begin{aligned} \frac{\partial \bar{\sigma}(\Delta)}{\partial \Delta_t} &= \frac{\partial \sigma_p(\Delta)}{\partial \Delta_t} + \frac{\partial \sigma_b(\Delta)}{\partial \Delta_t} \\ &= \sqrt{\frac{\tau E_f (l_0 + \Delta_t)^2}{\left[\sqrt{(l_0 + \Delta_t)^2 + (\Delta_n)^2} - l_0 \right] [(l_0 + \Delta_t)^2 + (\Delta_n)^2] d}} + \frac{E_f}{\delta/d} \left[\frac{-\Delta_n^2}{(l_0 + \Delta_t)^3} \right]. \end{aligned} \quad (\text{B.8})$$

Appendix C. Derivatives of the heat-conduction model

The derivatives of thermal conductance, h_{CZ} , with respect to the crack surface temperatures present in the Jacobian, \mathbf{J}_{th} , depend on terms representing the conductance due to gas, fiber and radiation. The derivatives of the gas conductance, h_g , fiber conductance, h_f , and conductance due to radiation, h_r , with respect to the crack surface temperatures are

$$\frac{\partial h_g}{\partial \theta_+} = \frac{\partial h_g}{\partial \theta_-} = \frac{(1 - V_f^{\text{C}}) C_g}{2 \Delta_n}, \quad (\text{C.1})$$

$$\frac{\partial h_f}{\partial \theta_+} = \frac{\partial h_f}{\partial \theta_-} = \frac{V_f^{\text{C}} C_f \sin \varphi}{2 \Delta_n}, \quad (\text{C.2})$$

$$\frac{\partial h_r}{\partial \theta_+} = \frac{S_b}{2/e_m - 1} [3(\theta_+ - \theta_0)^2 + 2(\theta_+ - \theta_0)(\theta_- - \theta_0) + (\theta_- - \theta_0)^2], \quad (C.3)$$

$$\frac{\partial h_r}{\partial \theta_-} = \frac{S_b}{2/e_m - 1} [3(\theta_- - \theta_0)^2 + 2(\theta_+ - \theta_0)(\theta_- - \theta_0) + (\theta_+ - \theta_0)^2]. \quad (C.4)$$

The derivatives of thermal conductance, h_{CZ} , with respect to normal Δ_n and tangential displacement jump Δ_t , present in the coupling Jacobian, \mathbf{J}_{tm} , are dependent on terms representing the conductance due to gas and fiber. The derivatives of the gas conductance, h_g , and fiber conductance, h_f , with respect to the displacement jumps are

$$\frac{\partial h_g}{\partial \Delta_n} = - \left[k_g + C_g \left(\frac{\theta_+ + \theta_-}{2} \right) \right] \left[\frac{1}{\Delta_n^2} + \frac{\pi d^2 n_0 l_0}{4} \left(\frac{1}{\Delta_n^2} \frac{\partial n(\Delta)}{\partial \Delta_n} - \frac{2n(\Delta)}{\Delta_n^3} \right) \right], \quad (C.5)$$

$$\frac{\partial h_g}{\partial \Delta_t} = - \left[k_g + C_g \left(\frac{\theta_+ + \theta_-}{2} \right) \right] \left[\frac{\pi d^2 n_0 l_0}{4 \Delta_n^2} \frac{\partial n(\Delta)}{\partial \Delta_t} \right], \quad (C.6)$$

$$\begin{aligned} \frac{\partial h_f}{\partial \Delta_n} = & \left[k_f + C_f \left(\frac{\theta_+ + \theta_-}{2} \right) \right] \left[\frac{\pi d^2 n_0 l_0}{4} \left(\frac{\sin \varphi}{\Delta_n^2} \frac{\partial n(\Delta)}{\partial \Delta_n} \right. \right. \\ & \left. \left. - \frac{2n(\Delta) \sin \varphi}{\Delta_n^3} + \frac{n(\Delta)}{\Delta_n^2} \frac{\partial \sin \varphi}{\partial \Delta_n} \right) \right], \end{aligned} \quad (C.7)$$

$$\frac{\partial h_f}{\partial \Delta_t} = \left[k_f + C_f \left(\frac{\theta_+ + \theta_-}{2} \right) \right] \left[\frac{\pi d^2 n_0 l_0}{4 \Delta_n^2} \left(\sin \varphi \frac{\partial n(\Delta)}{\partial \Delta_t} + n(\Delta) \frac{\partial \sin \varphi}{\partial \Delta_t} \right) \right]. \quad (C.8)$$

The derivatives of the number of fibers, $n(\Delta)$, with respect to the displacement jumps are expressed in Appendix B. The derivatives of $\sin(\varphi)$ with respect to the displacement jump are

$$\begin{aligned} \frac{\partial \sin \varphi}{\partial \Delta_n} &= \frac{\partial \sin[\tan^{-1}(\Delta_n/(l_0 + \Delta_t))]}{\partial \Delta_n} \\ &= \frac{1}{\sqrt{(l_0 + \Delta_t)^2 + (\Delta_n)^2}} - \frac{\Delta_n^2}{[(l_0 + \Delta_t)^2 + (\Delta_n)^2]^{3/2}}, \end{aligned} \quad (C.9)$$

$$\begin{aligned} \frac{\partial \sin \varphi}{\partial \Delta_t} &= \frac{\partial \sin[\tan^{-1}(\Delta_n/(l_0 + \Delta_t))]}{\partial \Delta_t} \\ &= - \frac{\Delta_n}{\sqrt{(l_0 + \Delta_t)^2 + (\Delta_n)^2}} + \frac{\Delta_n^3/(l_0 + \Delta_t)}{[(l_0 + \Delta_t)^2 + (\Delta_n)^2]^{3/2}}. \end{aligned} \quad (C.10)$$

References

- ABAQUS v6.3.1. HKS Inc., Pawtucket RI.
- Barber, J.R., 1979. Steady-state thermal stresses caused by an imperfectly conducting penny shaped crack in an elastic solid. *J. Therm. Stress.* 3, 77–83.
- Barber, J.R., Comninou, M., 1983. The penny-shaped interface crack with heat flow: 2. imperfect contact. *J. Appl. Mech.* 50, 770–776.
- Barenblatt, G.I., 1962. The mathematical theory of equilibrium cracks in brittle fracture. *Adv. Appl. Mech.* 7, 55–129.

- Benzeggagh, M.L., Kenane, M., 1996. Measurement of mixed-mode delamination fracture toughness of unidirectional glass/epoxy composites with mixed-mode bending apparatus. *Compos. Sci. Technol.* 56, 439–449.
- Brennan, J.J., Bentsen, L.D., Hasselman, D.P.H., 1982. Determination of the thermal conductivity and diffusivity of thin fibers by the composite method. *J. Mater. Sci.* 17, 2337–2342.
- Brockmeyer, J.W., 1993. Ceramic matrix composite application in advanced liquid fuel rocket engine turbomachinery. *J. Eng. Gas Turbines Power* 115, 58–63.
- Chao, C.K., Chang, R.C., 1994. Analytical solutions and numerical examples for thermoelastic interface crack problems in dissimilar anisotropic media. *J. Therm. Stress.* 17, 285–299.
- Chen, W.H., Huang, C.C., 1992. Three-dimensional thermal analysis of an infinite solid containing an elliptical surface crack. *Int. J. Fract.* 54, 225–234.
- Cox, B.N., 1994. Delamination and buckling in 3D composites. *J. Compos. Mater.* 28, 1114–1126.
- Cox, B.N., 1999. A constitutive model for through-thickness reinforcement bridging a delamination crack. *Adv. Compos. Lett.* 8, 249–256.
- Dimitrienko, Y.I., 1999. *Thermomechanics of Composites under High Temperatures*. Kluwer Academic Publishers, Dordrecht.
- Donaldson, K.Y., Trandell, B.D., Lu, Y., Hasselman, D.P.H., 1998. Effect of delamination on the transverse thermal conductivity of a SiC-fiber-reinforced SiC-matrix composite. *J. Am. Ceram. Soc.* 81, 1583–1588.
- Dransfield, K., Baillie, C., Mai, Y.-W., 1994. Improving the delamination resistance of CFRP by stitching—a review. *Compos. Sci. Technol.* 50, 305–317.
- Ducept, F., Davies, P., Gamby, D., 1997. An experimental study to validate tests used to determine mixed-mode failure criteria of glass/epoxy composites. *Compos. Part A* 28 A, 719–729.
- Florence, A.L., Goodier, J.N., 1959. Thermal stresses at spherical cavities and circular holes in uniform heat flow. *J. Appl. Mech.* 26, 293–294.
- Florence, A.L., Goodier, J.N., 1963. The linear thermoelastic problem of uniform heat flow disturbed by a penny-shape insulated crack. *Int. J. Eng. Sci.* 1, 540–553.
- Hasebe, N., Tamai, K., Nakamura, T., 1986. Analysis of kinked crack under uniform heat-flow. *J. Eng. Mech.* 112, 31–42.
- Hatta, H., Taya, M., 1985. Effective thermal conductivity of a misoriented short fiber composite. *J. Appl. Phys.* 58, 2478–2486.
- Hattiangadi, A., Siegmund, T., 2002. Bridging effects in cracked laminates under thermal gradients. *Mech. Res. Commun.* 29, 457–464.
- Heredia, F.E., Evans, A.G., Anderson, C.A., 1995. Tensile and shear properties of continuous fiber-reinforced SiC/Al₂O₃ composites processed by melt oxidation. *J. Am. Ceram. Soc.* 78, 2790–2800.
- Hutchinson, J.W., Evans, A.G., 2002. On the delamination of thermal barrier coatings in a thermal gradient. *Surf. Coat. Technol.* 149, 179–184.
- Hutchinson, J.W., Lu, T.J., 1995. Laminate delamination due to thermal gradients. *J. Eng. Mater. Technol.* 117, 386–390.
- Itou, S., 1993. Thermal stresses around a crack in an adhesive layer between two dissimilar elastic half-planes. *J. Therm. Stress.* 16, 373–400.
- Jansson, N.E., Larsson, R., 2001. A damage model for simulation of mixed-mode delamination growth. *Compos. Struct.* 53, 409–417.
- John, R., Zawada, L.P., Kroupa, J.L., 1999. Stresses due to temperature gradients in ceramic-matrix-composite aerospace components. *J. Am. Ceram. Soc.* 82, 161–168.
- Kaute, D.A.W., Shercliff, H.R., Ashby, M.F., 1993. Delamination, fiber bridging and toughness of ceramic matrix composites. *Acta Metall. Mater.* 41, 1959–1970.
- Kaute, D.A.W., Shercliff, H.R., Ashby, M.F., 1995. Modelling of fiber bridging and toughness of ceramic matrix composites. *Ser. Metall. Mater.* 32, 1055–1060.
- Krenkel, W., Henke, T., 1999. Design of high performance CMC brake discs. *Key Eng. Mater.* 164–1, 421–424.
- Kuo, A.Y., 1990. Effects of crack surface heat conductance on stress intensity factors. *J. Appl. Mech.* 57, 354–358.
- Lee, Y.D., Erdogan, F., 1998. Interface cracking of FGM coatings under steady-state heat flow. *Eng. Fract. Mech.* 59, 361–380.

- Lee, K.Y., Park, S.J., 1995. Thermal-stress intensity factors for partially insulated interface crack under uniform heat-flow. *Eng. Fract. Mech.* 50, 475–482.
- Lee, K.Y., Shul, C.W., 1991. Determination of thermal stress intensity factors for an interface crack under vertical heat-flow. *Eng. Fract. Mech.* 40, 1067–1074.
- Li, Z., Bradt, R.C., 1987. Thermal expansion and thermal expansion anisotropy of SiC polytypes. *J. Am. Ceram. Soc.* 70, 445–448.
- Llorca, J., Elices, M., 1992. A cohesive crack model to study the fracture behavior of fiber-reinforced brittle-matrix composites. *Int. J. Fract.* 54, 251–267.
- Lu, T.J., Hutchinson, J.W., 1995. Effect of matrix cracking on the thermal conductivity of fiber-reinforced composites. *Philos. Trans. Roy. Soc. London A* 351, 595–610.
- Martin-Moran, C.J., Barber, J.R., Comninou, M., 1983. The penny-shaped interface crack with heat flow: 1. perfect contact. *J. Appl. Mech.* 50, 29–36.
- McDonald, K.R., Dryden, J.R., Majumdar, A., Zok, F.W., 2000. Thermal conductance of delamination cracks in a fiber-reinforced ceramic composite. *J. Am. Ceram. Soc.* 83, 553–562.
- Miller, T.C., Chona, R., 1998. Finite element analysis of a thermally loaded interface crack in a ceramic coating. *Eng. Fract. Mech.* 59, 203–214.
- Mogro-Campero, A., Johnson, C.A., Bednarczyk, P.J., Dinwiddie, R.B., Wang, H., 1997. Effect of gas pressure on thermal conductivity of zirconia thermal barrier coatings. *Surf. Coat. Technol.* 94–95, 102–105.
- Mouritz, A.P., Cox, B.N., 2000. A mechanistic approach to the properties of stitched laminates. *Compos. Part A: Appl. Sci. Manuf.* 31, 1–27.
- Munro, R.G., 1997. Evaluated material properties for a sintered α -Al₂O₃. *J. Am. Ceram. Soc.* 80, 1919–1928.
- Nadeau, J.C., Ferrari, M., 1999. Microstructural optimisation of a functionally graded transversely isotropic layer. *Mech. Mater.* 31, 637–651.
- Needleman, A., 1987. A continuum model for void nucleation by inclusion debonding. *J. Appl. Mech.* 54, 525–531.
- Nemat-Nasser, S., Hori, M., 1999. *Micromechanics: Overall Properties of Heterogeneous Materials*, 2nd Edition. Elsevier, Amsterdam.
- Pantusa, D., Bathe, K.-J., Bouzinov, P.A., 2000. A finite element procedure for analysis of thermo-mechanical solids in contact. *Comput. Struct.* 75, 551–573.
- Partridge, I.K., Singh, S., 1995. Mixed-mode fracture in an interleaved carbon-fiber/epoxy composite. *Compos. Sci. Technol.* 55, 319–327.
- Qian, G., Nakamura, T., Berndt, C.C., 1998. Effects of thermal gradient and residual stresses on thermal barrier coating fracture. *Mech. Mater.* 27, 91–110.
- Rikards, R., Buchholz, F.-G., Wang, H., Bledzki, A.K., Korjakin, A., Richard, H.-A., 1998. Investigation of mixed mode I/II interlaminar fracture toughness of laminated composites by using a CTS type specimen. *Eng. Fract. Mech.* 61, 325–342.
- Sbaizero, O., Charalambides, P.G., Evans, A.G., 1990. Delamination cracking in laminated ceramic-matrix composite. *J. Am. Ceram. Soc.* 73, 1936–1940.
- Sih, G.C., 1962. On the singular character of thermal stresses near a crack tip. *J. Appl. Mech.* 29, 587–589.
- Simon, G., Bunsell, A.R., 1984. Mechanical and structural characterisation of the Nicalon silicon carbide fiber. *J. Mater. Sci.* 19, 3649–3657.
- Spearing, S.M., Evans, A.G., 1992. The role of fiber bridging in the delamination resistance of fiber-reinforced composites. *Acta Metall. Mater.* 40, 2191–2199.
- Tada, H., Paris, P.C., Irwin, G.T., 1973. *The Stress Analysis of Cracks Handbook*. Del Research Corp., MO, USA.
- Thouless, M.D., Evans, A.G., 1988. Effects of pull-out on the mechanical properties of ceramic-matrix composites. *Acta Metall.* 36, 517–522.
- Tivey, R., Ando, T., Antipenkov, A., Barabash, V., et al., 1999. ITER divertor design issues and research and development. *Fusion Eng. Des.* 46, 207–220.
- Touloukian, Y.S. (Ed.), 1967. *Thermophysical Properties of High Temperature Solid Materials*, Vol. 4. Macmillan, New York.

- Venkatesha, K.S., Ramamurthy, T.S., Dattaguru, B., 1996. Generalised modified crack closure integral and its application to interface crack problems. *Comput. Struct.* 60, 665–676.
- Volokh, K.Y., Needleman, A., 2002. Buckling of sandwich beams with compliant interfaces. *Comput. Struct.* 80, 1329–1355.
- Yan, G., Ting, T.C.T., 1993. The $r(-1/2)\ln(r)$ singularity at interface cracks in monoclinic and isotropic bimaterials due to heat-flow. *J. Appl. Mech.* 60, 432–437.
- Zavarise, G., Wriggers, P., Stein, E., Schrefler, B.A., 1992. A numerical model for thermomechanical contact based on microscopic interface laws. *Mech. Res. Commun.* 19, 173–182.